INVESTIGATION OF MAGNETIC PROPERTIES OF Fe_2MnP-BASED MATERIALS FOR REFRIGERATION USING DENSITY FUNCTIONAL THEORY

OTIENO VINCENT

A Thesis Submitted to the Graduate School in Partial Fulfillment of the Requirements for the Master of Science Degree in Physics of Egerton University

EGERTON UNIVERSITY

AUGUST, 2023

DECLARATION AND RECOMMENDATIONS

Declaration

This thesis is my original work and has not been presented in this university or any other for the award of a degree.
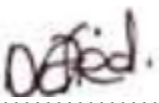
Signature…………………… Date…27/07/2023……

Otieno Vincent

SM13/14649/18

Recommendation

This thesis has been submitted with our approval as university supervisors.

Signature**: ………………** Date: ..27/07/2023..............

Dr. Winfred Mueni Mulwa (PhD)

Department of Physics

Egerton University

Signature: Date: ...27/07/2023.............

Dr. M.S. Kiplang'at Kirui (PhD)

Department of Physics

Egerton University

DEDICATION

This thesis is dedicated to my lovely and precious parents Peter Odhiambo Ng'ong'a and Alice Atieno Odhiambo, my brothers Kingsley, Bramwell and Javan and my sisters. It is also dedicated to all people who inspired and encouraged me through the academic milestone.

ACKNOWLEDGEMENTS

ABSTRACT

Increased campaign against environmental pollution and public awareness concerning global warming and food security has necessitated the efforts for reduction of emission of gases that adversely affect environment and deplete ozone layer. These gases include carbon (IV) oxide and chlorofluorocarbons, especially those emitted by compressed fluid refrigerators that are currently on the market. Alternative technologies are required to minimize or eliminate the emission of these harmful gases. Magnetocaloric effect (MCE), is a phenomenon related to the application and removal of varying magnetic field, which in turn shows changes in temperatures among selected magnetic materials. This effect forms the basis of a new alternative technology, magnetic refrigeration, a superior technology compared to compressed fluid refrigeration. However, many of the magnetic materials have been found to be structurally unstable, toxic and inefficient in terms of power consumption, hence not suitable to be magnetic refrigerants. Therefore, this study investigated the magnetic properties of stable iron-based compounds (Fe_2MnP-A (A= indium In, selenium Se, and tin Sn) under thermal and magnetic cycles as viable magnetic refrigerants. The properties investigated included absolute magnetization, total magnetization and magnetic phase transition. Parent compound had A as silicon which was later substituted with atoms of Se, Sn and In hence viable refrigerant which showed large MCE was modelled as the magnetic refrigerant. The compound has been shown to exhibit a magnetocaloric effect due to its magnetic nature and hence can be used as a magnetic refrigerant. The study reported was carried out using Density Functional Theory (DFT) as the modelling and simulation method of the material. This theory is a ground state method which aims at obtaining a structurally stable system. MCE phenomenon on structurally stable compound (Fe_2MnP-A (A= In, Se, and Sn) modelled by DFT was determined using first principle calculations. When Si was used at the A site, instability along the magnetic phase transition was observed. When indium, Se and Sn replaced silicon in FeMnPSi, it was observed that there was an effect in both total and absolute magnetization. Se and Sn showed a reduction in magnetic moment whereas In showed promising results by an increase in magnetic moment. The electronic band structure results indicated that they were all studied materials were metals. Antiferromagnetic states showed no net magnetic moments as the spin-polarized graph resulted in perfect symmetry of spin-up projected density of states (PDOS) and spin-down PDOS. From the thermo_pw calculations, it was realized that $FeMnP_{0.67} In_{0.33}$ is the best candidate for magnetic refrigeration among the studied compounds.

TABLE OF CONTENTS

LIST OF FIGURES

LIST OF TABLES

LIST OF ABBREVIATIONS AND ACRONYMS

a.u	atomic units
AFM	Anti-FerroMagnetic
BFGS	Broyden, Fletcher, Goldfarb and Shannon
CB	Conduction Band
Celldm	Cell dimension
DFT	Density Functional Theory
DOS	Density of State
EOS	Equation of State
FM	FerroMagnetic
GGA	Generalized Gradient Approximation
GRACE	Graphing Advanced Computing and Exploration of data
IBZ	Irreducible Brillouin zone
MCE	Magnetocaloric Effect
PAW	Projected augmented wave
PBE	Perdew Burke Ernzerhof
PM	Paramagnetic
PP	Pseudopotentials
Pw	Plane waves
PDOS	Projected Density of State
Pwscf	Plane-wave self-consistent field
Q.E	Quantum ESPRESSO
SCF	Self-consistent field
USPP	Ultra-soft pseudopotential
VB	Valence Band
VESTA	Visualization system for electronic and structural analysis

LIST OF SYMBOLS

ΔS   Isothermal change in entropy due to magnetic field change

ΔT   Adiabatic temperature variation as a result of change magnetic field

E_{xc} Exchange and Correlation energy of interacting system

E_{cut} Plane wave cutoff energy

Fe   Iron

$F_{[n(r)]}$ Functional of density

Gd   Gadolinium

MCE   Magnetocaloric effect

M_A mass of the nucleus A

$n_{(r)}$ Electron charge density

$\boldsymbol{\Psi}$ wave function

P   Phosphorous

V_{ae} All-electron potential

$V_{e\text{-}e}$ Electron-electron Potential energy Gradient

Δ   operator/Laplacian operator

CHAPTER ONE

INTRODUCTION

1.1 Background information

Magnetocaloric effect (MCE), is a magneto-thermodynamic phenomenon in which a reversible change in temperature of a suitable magnetic material is caused by exposing the material to a varying magnetic field. Over the years this mechanism has been called adiabatic demagnetization by low-temperature scientists due to its applications in low-temperature processes specifically temperature drop. The magnetocaloric effect was discovered back in the year 1881, this was when Warburg observed it in iron elements (Taskaev *et al.,* 2016; Warburg, 1881;). The origin of the MCE was later explored and explained independently by Debye (1926) and Giauque (1927). They developed the first practical use of the MCE; referred to as the adiabatic demagnetization used to reach temperatures lower than that of liquid helium. Currently, there is a great deal of interest in using the MCE as an alternative technology for refrigeration, from room temperature to the temperatures of hydrogen and helium liquefaction (~20 - 4.2 K). Magnetic refrigeration offers the prospect of an energy-efficient and environment-friendly alternative to the common vapour-cycle refrigeration technology in use today (Gschneidner & Pecharsky, 2000; Pecharsky & Gschneidner, 1999).

In MCE refrigeration process, a decrease in the strength of an externally applied magnetic field allows the magnetic domains of a chosen (magnetocaloric) material to become disoriented from the magnetic field by the agitating action of the thermal energy (phonons) present in the material. In an isolated system, no energy is allowed to move into the material during this process (i.e. an adiabatic process), the temperature drops as the domains absorb the thermal energy to perform their reorientation.

MCE is shown in some chemical elements like gadolinium, Gd and some of its alloys. Gadolinium's temperature is observed to increase when it enters certain magnetic fields. When it leaves the magnetic field, the temperature returns to normal. The effect is considerably stronger for the gadolinium alloy $Gd_5(Si_2Ge_2)$ (Gombi & Sahu, 2020). Praseodymium alloyed with nickel (PrNi5) has such a strong MCE effect that it has allowed scientists to approach within one-thousandth of a degree of absolute zero. Gadolinium element and some of its alloys are realized to

be soluble hence the need to replace it with another appropriate refrigerant material (Ekanth & Kishor, 2016).

1.2 Statement of the problem

Improving energy efficiency, minimisation of energy consumption, and reducing the ozone layer depletion and global warming is the target of developing countries today. The high energy consumption in the domestic market is household appliances such as refrigerators and air conditioners. These household appliances are products of refrigeration technology that depend on refrigerants such as chlorofluorocarbons, hydro-fluorocarbons and other chemicals to complete vapour-compression refrigeration cycle. In the process, there is an emission of carbon (IV)oxide (CO_2) into the environment. The emission of this gas into the environment leads to the effect of ozone layer depletion hence global warming. Therefore, there is a need to replace the current cooling technologies that depend on compression and expansion of vapour with a more energy-efficient cooling technology to reduce ozone layer depletion and global warming. Magnetic refrigeration is one of the upcoming technologies which can be used to replace the existing air compression refrigeration processes. Magnetic refrigerant must be magnetic. Density functional theory is a cheap modelling technique that is used by researchers to model and predict the properties of materials.

1.3 Objectives

1.3.1. General objective

Investigation of magnetic properties of Fe_2MnP-based materials for near-room-temperature refrigeration.

1.3.2 Specific objectives

i.   To determine the effect of doping stable phases of Fe_2MnP with silicon element on the magnetic properties for refrigeration.

ii. To determine the effect of substitutional elements (A= In, Se, Sn) on the magnetic properties of stable phases of Fe_2MnP-A during refrigeration.

iii. To determine the effect of substitutional elements (A= In, Se, Sn) on the magnetic-elastic transition susceptibility of stable phases of Fe_2MnP-A during refrigeration.

1.4 Research questions

i. What is the effect of doping the stable phase of FeMnP with silicon on the magnetic properties as a refrigerant?

ii. What is the effect of substitutional elements (A= In, Se, Sn) on the magnetic properties of stable phases of Fe2MnP-A during refrigeration?

iii. What is the effect of substitutional elements (A= In, Se, Sn) on the magnetic-elastic transition susceptibility of stable phases of Fe2MnP-A during refrigeration?

1.5 Justification

In this study, a theoretical study of $FeMnP_{1-x}(Si, In, Se, Sn)_x$ (x =0.33) was done. Magnetic properties of stable structures from $FeMnP_{1-x}(Si)_x$ (x = 0.33) and $FeMnP_{1-x}A_x$ (A = In and Se, x = 0.33) were determined. One of the available options for optimisation of the mechanical stability of magnetocaloric materials was by alloying/replacing the atoms at the A site in $FeMnP_{1-x}A_x$ (in this case A = Si) with viable elements that are non-toxic. The primary aim of alloying/replacement was to mimic the bonding between atoms which could eventually affect the mechanical stability, magnetic behaviour, and transition order and decreases the thermal hysteresis. Therefore, a careful characterisation of the alloying/replacement for such compositions was essential to determine both the stable structures and their electronic properties, leading ultimately to a better understanding of their mechanical stability concerning their usefulness as magnetocaloric materials. The modelled refrigerant had the following advantages.

1. This modelled magnetic refrigerant is less harmful to the environment since it is non-toxic and does not emit carbon (IV) oxide gas during the refrigeration process.

2. The energy consumption of the device is much low since it only needs pair of magnets to provide a magnetic field.

1.6 Scope and Limitations

This study was carried out using DFT formalism as instigated by the QE code. It was purely theorical calculations. The study assumed that the DFT approach gives an accurate prediction of the experimental findings.

<div align="center">**CHAPTER TWO**</div>

<div align="center">**LITERATURE REVIEW**</div>

2.1 Theory of magnetocaloric effect (MCE)

To explicate the origin of the MCE, we use thermodynamics, which stretches the relationship between the magnetic variables (magnetisation of material and magnetic field) to temperature and entropy. It is worth observing that all magnetic materials intrinsically show MCE (Dong *et al.*, 2020), although the strength of the effect depends on the diverse properties of each material. The physical origin of the MCE is the coupling of the magnetic sublattice to the applied magnetic field, H, which vagaries the magnetic input to the entropy of the solid. The value of the entropy of a ferromagnet (FM) at constant pressure depends on both H and temperature, T, whose contributions are the lattice (S_{lat}) and electronic (S_{el}) entropies, as for any solid, and the magnetic entropy (S_m) (Silva, 2017). Which is presented by equation 2.1.

$$S(T, H) = S_m(T, H) + S_{lat}(T) + S_{el}(T) \hspace{3cm} 2.1$$

It can be deduced that:

(i) Once the magnetic field is applied adiabatically (i.e., the system is isolated consequently total entropy remains constant) in a reversible process, the magnetic entropy reduces, and the total entropy does not change, i.e.,

$$S(T_0, H_0) = S(T_1, H_1) \hspace{3cm} 2.2$$

then, the temperature rises. This increase in temperature adiabatically can be visualised as the isentropic variance between the corresponding S (T, H) functions and it is a measure of the MCE in the material (Villarreal, 2016).

$$\Delta T_{ad} = T_1 - T_0 \hspace{3cm} 2.3$$

(ii) On application of the magnetic field isothermally (Temperature T, remains constant), the total entropy reduces due to the decline in the magnetic contribution, and therefore the entropy change in the process is defined by equation 2.4.

$$\Delta S_m = S(T_0, H_0) - S(T_0, H_1) \hspace{3cm} 2.4$$

Mutually the adiabatic temperature change, ΔT_{ad}, and the isothermal magnetic entropy change, ΔS_m, are characteristic values of the MCE. Both quantities are functions of the initial temperature, T_o, and the magnetic field variation (Hao *et al.,* 2005),

$$\Delta H = H_1 - H_0 \qquad\qquad 2.5$$

Therefore, it is straightforward to see that if rising in the field upsurges magnetic order (decreases magnetic entropy), then ΔT_{ad} (T; ΔH) is positive and it applies that the magnetic solid warms up, while ΔS_m (T, ΔH) is negative consequential to a temperature reduction of the material. But if the field is reduced, magnetic order decreases and ΔT_{ad} (T, -ΔH) is thus negative, while ΔS_m (T, -ΔH) is positive, giving rise to a cooling of the magnetic solid. The relation between H, the magnetisation of the material, M, and T, to the MCE values, ΔT_{ad} (T, ΔH) and ΔS_m (T ΔH), is given by one of the Maxwell relations (Samanta *et al.,* 2015).

$$\left(\frac{\partial S(H,T)}{\partial H}\right)_T = \left(\frac{\partial M(H,T)}{\partial T}\right)_H \qquad\qquad 2.6$$

Integrating equation 2.6 for an isothermal (and isobaric) process, we obtain

$$\Delta S_m(T, \Delta H) = \int_{H1}^{H2} \left(\frac{\partial M(H,T)}{\partial T}\right)_H dH \qquad\qquad 2.7$$

Equation 2.7 illustrates that the magnetic entropy change is proportional to both the derivative of magnetisation concerning temperature at a constant field and to the field variation. Using the following thermodynamic relations (Samanta *et al.,* 2015).

$$\left(\frac{\partial T}{\partial H}\right)_S = -\left(\frac{\partial S}{\partial H}\right)_T \left(\frac{\partial T}{\partial S}\right)_H \qquad\qquad 2.8$$

$$C_H = T\left(\frac{\partial S}{\partial T}\right)_H$$

where C_H is defined as the heat capacity at a constant field, and taking into account equation 2.6, the infinitesimal adiabatic temperature change is given by equation 2.9

$$(dT)_{ad} = -\left(\frac{T}{C(T,H)}\right)_H \left(\frac{\partial M(H,T)}{\partial T}\right)_H dH \qquad\qquad 2.9$$

After integrating this equation 2.9, an expression obtained characterises the MCE,

$$\Delta T_{ad}(T, \Delta H) = -\int_{H1}^{H2} \left(\frac{T}{C(T,H)}\right)_H \left(\frac{\partial M(H,T)}{\partial T}\right)_H dH \qquad\qquad 2.10$$

By analysing equations. 2.9 and 2.10, some information about the behaviour of the MCE in solids can be expanded:

1. Magnetisation at a constant field in both paramagnets (PM) and simple FMs materials decreases with rising temperature, $\left(\frac{\partial M}{\partial T}\right)_H < 0$. Hence ΔT_{ad} (T, ΔH) should be positive, while ΔS_m (T, ΔH) should be negative for positive field changes, $\Delta H > 0$.

2. In FMs, the absolute value of the derivative of magnetisation for temperature, $\left|\left(\frac{\partial M}{\partial T}\right)_H\right|$ is maximum at T_c, and therefore $|\Delta S_m$ (T; ΔH) | should show peak at T = T_c.

The study into magnetic refrigeration has led to the unearthing of magnetic materials with exceptional temperature variation when they are adiabatically magnetised around room-temperature (Franco *et al.*, 2018; Pecharsky *et al.,* 1997;).

In rare-earth-based materials like Gadolinium, Gd metal, Gd$_5$ (Ge$_{1-x}$Si$_x$)$_4$ and La (Fe, Si)$_{13}$, a giant MCE has been observed (Franco *et al.*, 2018). Gadolinium and its compounds are found to be soluble in water and this makes them less appropriate in application as solid-state refrigerants (Franco *et al.*, 2018). In this instance, the choice is an electronic process relating to the magnetisation and demagnetisation of magnetic materials known as magnetic refrigeration that banks on the magnetocaloric effect (MCE) (Kotelnikova *et al*., 2015). In refrigeration technology, magnetic cooling which hinges on the MCE is usually used in refrigerators to achieve extremely low temperatures. Magnetic freezing has a higher cooling efficiency, low energy consumption, more compact and environmentally friendly when compared with vapour-compression refrigeration. Magnetic refrigeration does not depend on the uses of harmful and ozone-depleting coolant gases as reported by Viglione (2020). This agreed with Polvani *et al.* (2020) findings which realised that harmful gases cause ozone layer depletion.

Although, these rare-earth-based materials encompass expensive rare-earth metals which limit their application in practical devices (Behrsing *et al.,* 2014). There are other capable materials such as β-MnAs, Heusler alloys and Fe$_2$MnP-based compounds as shown in figure 2.1. The β-MnAs compound contains a toxic element (As) and has poor mechanical properties (Franco *et al.*, 2018). Nevertheless, the Heusler alloys and Fe$_2$MnP-based compounds do not contain expensive and toxic elements, these make them more substantial and essential as magnetocaloric materials (Cicek *et al.*, 2020). The FeMn-based magnetocaloric materials of the form FeMnP$_{1-x}$A$_x$ (A = As, Si, Ge and Ga) with hexagonal Fe$_2$MnP-based structures as shown in figure 2.1 are some of the studied compounds for magnetic refrigeration (Ma *et al.,* 2017).
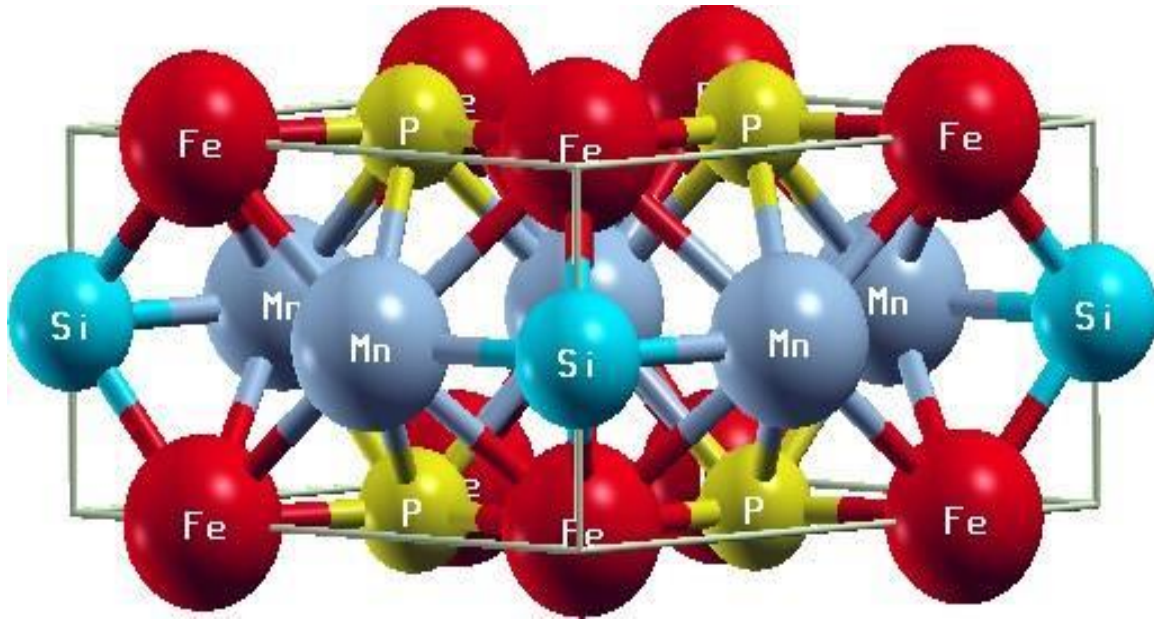
Figure 2. 1: Crystal structure of FeMnP0.67Si0.33 (Source; Xcrysden software)

It has been noticed that close to room temperature, this group of materials, exhibit first order magneto-elastic transition (Ma *et al.,* 2017) which leads to changes in the ratio of the lattice parameters (c/a) without significant changes in the volume. Their elevated performance at the curie temperature T_c hinge on the frequency of the magnetic and the elastic transition at the same time (Kaneyoshi *et al*., 2020). Examples in this route can be found for Ge and Ga replacement of A in FeMnP$_{1-x}$A$_x$ in a recent study (Ma *et al*., 2017), where it was established through their DFT calculations that FeMnP$_{0.66}$Ga$_{0.33}$ is mechanically and dynamically stable in both ferromagnetic and paramagnetic states which is similar to FeMnP$_{0.66}$Ge$_{0.33}$. Building on this example, this work extended the study to FeMnP$_{1-x}$Sn$_x$ (x = 0.33), FeMnP$_{1-x}$(In)$_x$ (x = 0.33), FeMnP$_{1-x}$(Se)$_x$ (x = 0.33) and FeMnP$_{1-x}$(Si)$_x$ (x = 0.33). In the last four structures, a supercell of 1 x 1 x 2 was constructed to model their structures.

Aimed at better practical device applications, many efforts have been made to improve the performance of these compounds (Ma *et al.,* 2017; Roy *et al.,* 2016) through modifications of the transition temperature, crystal parameters, hysteresis, transition order and magnetic properties (Roy *et al.,* 2016) by varying the ratio of the transition metals (Fe: Mn) respectively. Alternative choice implemented in experiments was doping with elements such as (Co, Ni, Cu, Cr, etc.) (Ou 2013).

FeMnP$_{1-x}$Si$_x$ from the group of FeMnP$_{1-x}$A$_x$ (A = As, Si, Ge, Ga) with hexagonal Fe$_2$MnP-based structure has been discovered as a likely candidate for good performance in magnetic refrigeration with a reduction in thermal hysteresis to around 1K. But then again, its weak mechanical stability along the phase transition restricts its application in real devices. Since a good magnetocaloric material is vital to be mechanically stable because of its function under recurring magnetic and thermal cycles, there is a need to alloy and replace Si atoms with other feasible elements to mimic the bonding between atoms (Ma *et al.,* 2017; Roy *et al.,* 2016). These results agreed to Hu *et al.* (2014) who realised the instability of silicon as a dopant in the magnetic material. The silicon atom causes mechanical instability of the compound FeMnPSi as a refrigerant, thus limiting its application in practical devices.

2.2 Near room temperature MCE

The prototypical material at room temperature is Gd, a rare earth metal which orders FM at T_c = 294 K. This lanthanide element has been broadly studied (Dan'kov *et al.,* 2000; Madireddi, 2010; Pecharsky *et al.,*1999; Tishin *et al.,* 1999), and ΔT_{ad} values at T_c are $\sim$6, 12, 16 and 20 K for magnetic field changes $\mu_0\Delta H$ = 2, 5, 7.5 and 10 T, respectively, which leads to a field condition of the MCE of$\sim$3 K/T at low fields, that decreases to $\sim$2 K/T at a higher magnetic field. A variety of alloys with Gd and other rare-earth metals have been fortified to improve the MCE in Gd. Gd-RX alloys, with RX = lanthanide (Tb, Dy, Er, Ho...) (Smaili & Chahine, 1997) and/or Y have been studied, but the alloying only decreases T_c which is undesirable, subsequently we advance from room temperature, while the MCE value does not surge noticeably for pure Gd. The only exemptions are nanocrystalline GdY alloys, which increase the MCE in Gd at $\mu_0\Delta H$ = 1 T (Gschneidner *et al.,* 2000). Most intermetallic compounds that order magnetically near room temperature and above$\sim$290 K show a prominently lower MCE than that of Gd element. For instance, Y2Fe17, with T_c $\sim$310 K, have been reported to yield a value of MCE which is significantly about 50% of that in Gd (Shao *et al.,* 1996). The same magnitude is about measured in Nd2Fe17 (Shao *et al.,* 1996), with T_c $\sim$324 K. It has been recommended that (Pr1:5Ce0:5)Fe17 could have MCE greater than that of Gd, but it has not been diverse empirically (Toliński *et al.,* 2012).

2.3 Measurement of the magnetocaloric effects (MCE)

There are two types of MCE extent explored in this study, that is direct measurement and indirect measurement.

2.3.1 Direct measurements

Direct methods to quantify MCE always encompass the measurement of the primary temperature (T_0) and final temperature (T_F) of the model under study, when the external magnetic field is varied from an initial value (H_0) to a final value (H_F). Then the measurement of the adiabatic temperature variation is basically given by equation 2.11

$$\Delta T_{ad}(T_0, H_F - H_0) = T_F - T_0 \qquad\qquad 2.11$$

Direct measurement method can be achieved by using both contact and non-contact techniques, depending on whether or not the temperature sensor is directly coupled to the model.

To accomplish direct measurements of MCE, a swift change of the magnetic field is required. Consequently, the measurements can be carried out either on immobilised samples by fluctuating the field (Franco *et al*., 2012) or by moving the sample in and out of a region of constant magnetic field (Gopal *et a*l., 1997). When electromagnets are employed in the experiment, then, the magnetic field is generally decreased to a value less than 2 T. When the model or the magnet is moved, permanent or superconducting magnets are usually employed, with a magnetic field range of 0.1 to 10 T. The precision of the direct experimental procedures be contingent on the errors in thermometry and field setting, the excellence of thermal insulation of the model, and the possible adjustment of the interpretation of the temperature sensor owing to the applied field (Gomès *et al.,* 2015).

2.3.2 Indirect measurements

Contrasting to direct measurements, which generally only yield the adiabatic temperature change, indirect experimentations allow the calculation of both ΔT_{ad} (T, ΔH) and ΔS_m (T, ΔH) in the case of heat capacity measurements, or just ΔS_m (T, ΔH) in the case of magnetisation measurements. In the latter circumstance, magnetisation must be measured as a function of T and H. This permits us to obtain ΔS_m (T, ΔH) by numerical integration of Equation 2.7, and it is very useful as a quick search for possible magnetic refrigerant materials (Franco *et al*., 2012). The precision of ΔS_m(T, ΔH) calculated from magnetisation data hinge on the precision of the measurements of the magnetic moment, T and H. It is also pretentious by the fact that the exact differentials in Equation 2.7 (dM, dH and dT) are replaced by the measured variations (ΔM, ΔT

and ΔH). Taking into account all these properties, the fault in the value of $\Delta S_m(T, \Delta H)$ lies within the range of 3-10% (Foldeaki *et al.,* 1997; Pecharsky *et al.,* 1999). The measurement of the heat capacity as a function of temperature in constant magnetic fields and pressure, $C(T)_{P,H}$, provides the most complete characterisation of MCE in magnetic materials. The entropy of a solid can be calculated from the heat capacity:

$$S(T)_{H=0} = \int_0^T \frac{C(T)_{P,H=0}}{T} dT + S_0 \qquad 2.12$$

$$S(T)_{H\neq0} = \int_0^T \frac{C(T)_{P,H}}{T} dT + S_{0,H} \qquad 2.13$$

where S_0 and $S_{0,H}$ are the zero temperature entropies. In a condensed system $S_0 = S_{0H}$. Hence, if S $(T)_H$ is known, both $\Delta T_{ad}(T, \Delta H)$ and $\Delta S_m(T, \Delta H)$ can be determined. Though, this valuation is not effective if a first-order transition occurs within the valuated range since the value of C_P is not deprived of at a first-order transition (Pecharsky & Gschneidner,1999; Pecharsky *et al.,* 2001). In this situation, the entropy curves show a discontinuity, which resembles to the entropy variation of the transition.

The entropy gap can be attained from different trial data, such as magnetisation and then the resultant $S(T)_H$ functions can be modified accordingly (Pecharsky & Gschneidner,1999). The precision in the dimensions of MCE using heat capacity data be contingent critically on the accuracy of $C(T)_{P,H}$ measurements and data exemption, both $\Delta T_{ad}(T,\Delta H)$ and $\Delta S_m(T, \Delta H)$ are minor deviations between two large values (temperatures and total entropies). The fault in $\Delta S_m(T, \Delta H)$, $\sigma[\Delta S_m(T, \Delta H)]$, calculated from heat capacity is given by the expression 2.14 (Vollmer & Mollmann, 2017)

$$\sigma[\Delta S_m(T, \Delta H)] = \sigma[S(T, H = 0)] + \sigma[S(T, H \neq 0)] \qquad 2.14$$

where $\sigma S(T, H = 0)$ and $\sigma S(T, H \neq 0)$ are the deviations in the calculation of the zero-field and non-zero field entropies respectively. The fault in the value of the adiabatic temperature change, $\sigma[\Delta T_{ad}(T, \Delta H)]$, is also relative to the errors in the entropy, but it is inversely proportional to the derivative of the entropy with respect to temperature (Pecharsky *et al.,* 1996):

$$\sigma[\Delta T_{ad}(T, \Delta H)] = \frac{\sigma[S(T,H=0)]}{\left(\frac{ds(T,H=0)}{dT}\right)} + \frac{\sigma[S(T,H\neq0)]}{\left(\frac{ds(T,H\neq0)}{dT}\right)} \qquad 2.15$$

It is worth noting that Equations. 2.14 and 2.15 yield the absolute error in MCE measurements and, hence, the relative errors strongly heave for small MCE values. Presumptuous that the precision of the heat capacity measurements is not field-dependent, the relative error in both ΔT_{ad} (T, ΔH) and ΔS_m (T, ΔH) is reduced for larger ΔH values.

2.4 Magnetic refrigeration

Presently, there is a great deal of attention in utilising the MCE as an alternate technology for refrigeration both in ambient and cryogenic temperatures (Harutyunyan, 2004). Magnetic refrigeration is an environmentally friendly cooling technology. It does not use ozone-depleting chemicals (such as chlorofluorocarbons), hazardous chemicals (such as ammonia), or greenhouse gases (hydrochlorofluorocarbons and hydrofluorocarbons). This was reported by Hessell (2013) whose investigation realised that gas compression refrigerators contribute to ozone layer depletion.

Most modern refrigeration systems and air conditioners still use ozone-depleting or global-warming volatile liquid refrigerants (Hessell, 2013; Pal *et al.,* 2018). Magnetic refrigerators use a solid refrigerant (usually in the form of spheres or thin sheets) and common heat transfer fluids (e.g. water, water-alcohol solution, air, or helium gas) with no ozone-depleting and/or global warming effects. Another significant difference between vapour-cycle refrigerators and magnetic refrigerators is the amount of energy loss incurred during the refrigeration cycle. Even the newest most efficient commercial refrigeration units operate well below the maximum theoretical (Carnot) efficiency, and few, if any, further improvements may be possible with the existing vapour-cycle technology (McLinden *et al.*, 2017).

Magnetic refrigeration, however, is fast becoming competitive with conventional gas compression technology because it bids considerable operating cost savings by eliminating the most inefficient part of the refrigerator, the compressor. The cooling efficiency of magnetic refrigerators working with Gd has been shown (Pecharsky *et al.,* 1999) to reach 60% of the Carnot limit, compared to only about 40% in the best gas-compression refrigerators. However, with the currently available magnetic materials, this high efficiency is only realised in high magnetic fields of 5 T. Therefore, research for new magnetic materials displaying larger MCE, which then can be operated in lower fields of about 2 T that can be generated by permanent magnets, is very significant (Zvyagin, 2017). The heating and cooling that occurs in the magnetic refrigeration technique is proportional to the size of the magnetic moments and the applied magnetic field. This

is why research in magnetic refrigeration is at present almost exclusively conducted on superparamagnetic materials and rare-earth compounds (Hamad *et al.*, 2015).

Refrigeration in the sub-room temperature (∼250-290 K) range is of particular interest because of the potential impact on energy savings and environmental concerns. As described in this chapter, materials to be applied in magnetic refrigeration must present a series of properties (Vázquez, 2015).

i. A first-order field-induced transition around the working temperature, to utilise the associated entropy change.

ii. A high refrigerant capacity, q, is a measure of how much heat can be transferred between the cold and hot sinks in one ideal refrigeration cycle, and it is calculated as:

a. $q = \int_{Tcold}^{Thot} \Delta S(T)_{\Delta H} \, dT$ 2.16

Therefore, a large entropy change in a temperature range as wide as possible is needed. (Pecharsky *et al.,* 2001).

iii. A low magnetic hysteresis, to avoid magnetic-work losses due to the rotation of domains in a magnetic refrigeration cycle.

iv. A low heat capacity C_p, since a high C_p increases the thermal load and more energy is required to heat the sample itself and causes a loss in entropy, for a given ΔS, ΔT_{ad} will be lower.

v. Low cost and non-toxic. The main problem of the rare-earth-based compounds, which are usually the best magnetic refrigerants in the whole temperature range (including pure Gd at room temperature) is their high cost.

In particular, the lately reported manganese arsenide (MnAs)-based materials show good predictions (Wada & Tanabe, 2001). However, the presence of Arsenic (As) in these compounds, which is bio lethal, could make them useless for commercial applications. Another type of compound, $La(Fe_xSi_{1-x})_{13}$, also presents a large MCE at room temperature, it has a low cost and is non-toxic (Franco *et al.,* 2012).

Schematic depiction of a magnetic-refrigeration cycle indicated in figure 2.2, illustrates heat transmission from the heat load to its environs. Light and dark grey depict the magnetic material without and with applied magnetic fields, respectively. Initially, disordered magnetic moments are arranged by a magnetic field, resulting in the heating of the magnetic material (Dennis *et al.,* 2013).

This heat is removed from the material to its surroundings by a heat-transfer medium. On removing the field, the magnetic moments randomise, which leads to the cooling of the magnetic material below the ambient temperature. Heat from the system is therefore dissipated using a heat-transfer medium (Zhao *et al*., 2012).
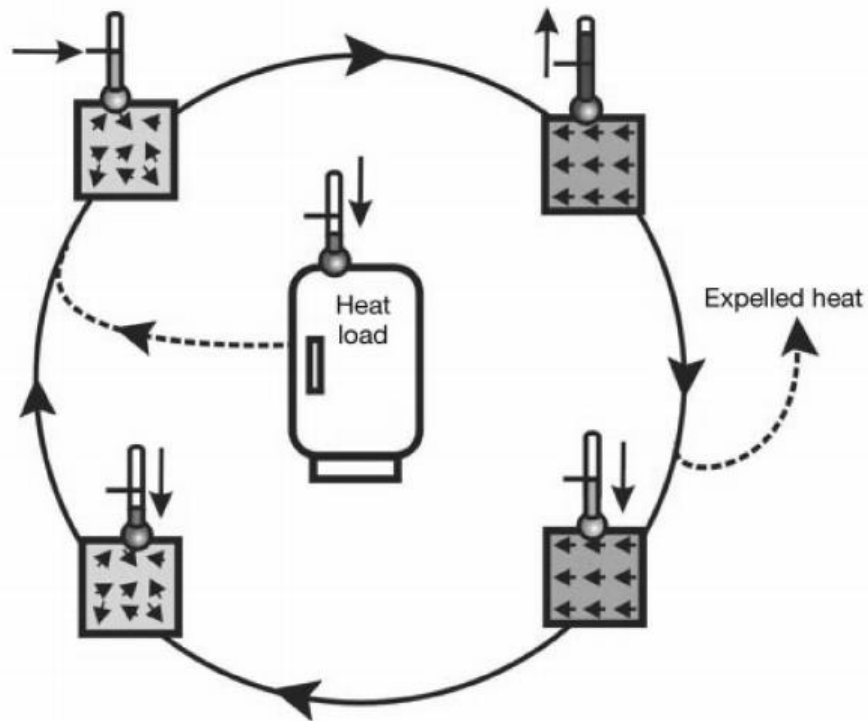
Figure 2. 2: Magnetic-refrigeration cycle

Source: Dennis et al. (2013)

2.5 Construction and working principle of magnetic refrigerator

Construction and systematic function of a magnetic fridge which employees MCE phenomenon is shown in figure 2.3. It is a demonstration of some of the important components of the system.

2.5.1 Required components and functions

i.   Magnets
ii. Hot Heat exchanger
iii. Cold Heat Exchanger
iv. Drive
v.   Magnetocaloric wheel
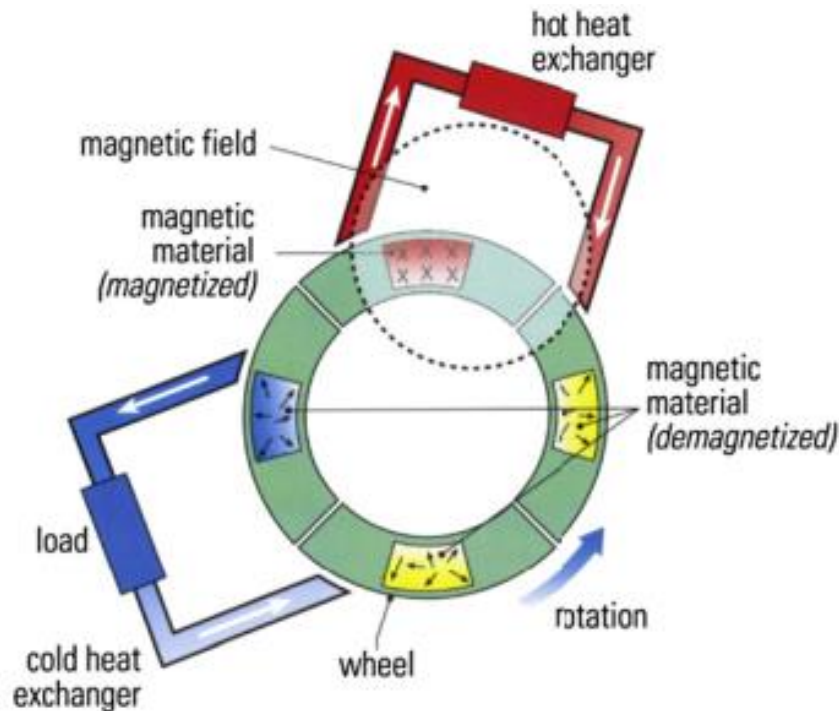
Figure 2. 3: Magnetic-refrigeration cycle in a magnetic field

Source: Dennis et al. (2013)

Magnets are the main functioning elements of magnetic refrigeration; they provide the magnetic field to the magnetic material serving as refrigerant so that they can lose heat to the surroundings or from the space to be cooled. Hot heat exchanger drains the heat from the refrigerant and emits it off to the surrounding (Tura *et al.,* 2011).

Cold heat exchanger absorbs the heat from the sample to be cooled and transfer it to the magnetic material while the drive provides the right rotation to the heat thus heat drifts in the right favorite direction. Magnetocaloric wheel joins the two magnets to work properly (Zimm *et al.,* 2006).

2.5.2 Working principle

Figure 2.4 (Bohigas *et al.,* 2000) is an illustration of temperature change when the magnetic material is positioned in the magnetic field, the thermometer attached to the magnetic material shows a temperature increase. But on the other side when the magnetic material is removed from

the magnetic field, the thermometer shows low temperature as its temperature reductions (Zvyagin, 2017).
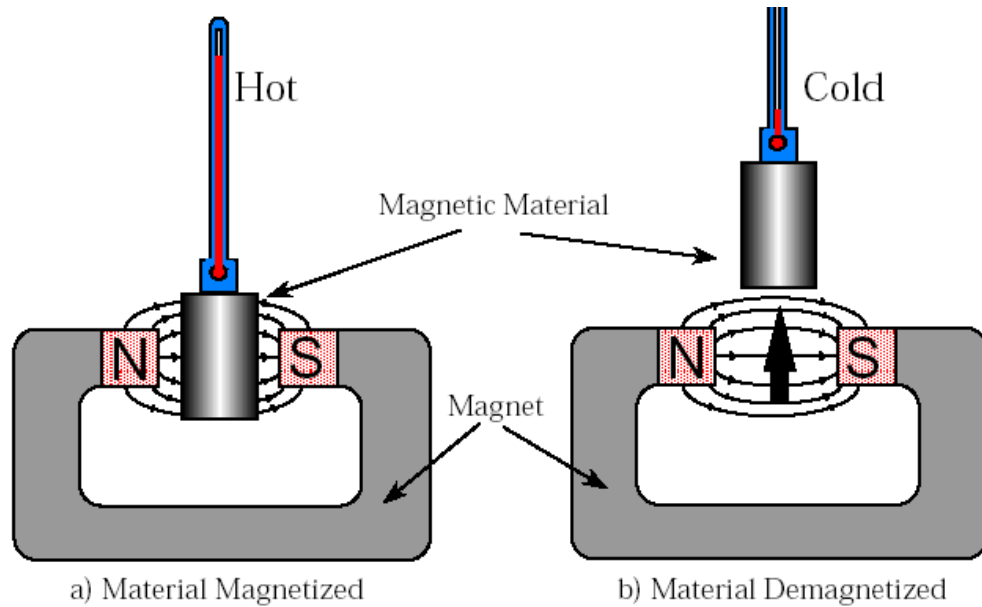
Figure 2. 4: a and **b**, Temperature change of magnetic material in magnetic field

Source: Bohigas et al. (2000)

(a)   (b)
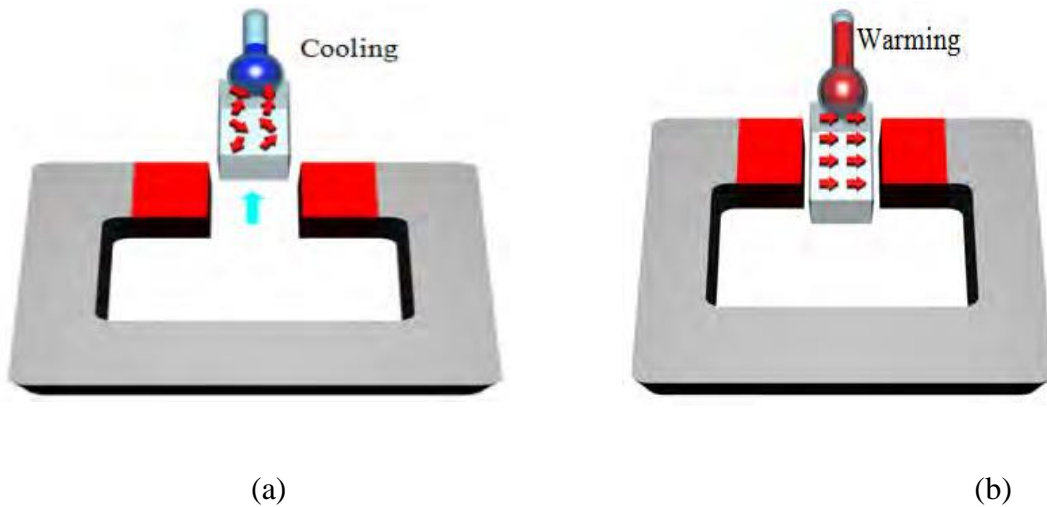
Figure 2. 5: a and **b,** Magnetic moments and temperature change during magnetisation and demagnetisation

Source: Bohigas et al. (2000)

Magnetic refrigeration is mainly based on MCE according to which some materials change in temperature when they are magnetized and demagnetised (Li *et al.,* 2021). Near the phase transition of the magnetic materials, the adiabatic application of a magnetic field decreases the

magnetic entropy by ordering the magnetic moments (Brück *et al.,* 2003). This agreed with the findings of Bohigas *et al.* (2002). This results in a temperature upsurge of the magnetic material.

This phenomenon is practically reversible for some magnetic materials; thus, adiabatic removal of the field reverts the magnetic entropy to its original state and cools the material accordingly. This reversibility combined with the ability to create devices with inherent work recovery makes magnetic refrigeration a potentially more efficient process than gas compression and expansion. The efficiency of magnetic refrigeration can be as much as 50% greater than for conventional refrigerators (Gómez *et al.,* 2013).

2.5.3 Proper functioning

When a fluctuating magnetic field is applied to the material, its temperature increases, and it will absorb heat from a sample to be cooled. When magnetic material is withdrawn from a magnetic field, it will lose heat as its temperature decreases and hence the cycle repeats over and again to provide the cooling effect at the desired place.

2.6 Magnetic materials

Only a limited number of magnetic materials possess a large enough MCE to be used in practical refrigeration systems. The search for better materials is focused on rare earth metals, either in pure form or combined with other metals into alloys and compounds (Balli *et al.,* 2012). The MCE is an intrinsic property of a magnetic solid. This thermal response of a solid to the application or removal of magnetic fields is maximised when the solid is near its magnetic ordering temperature (Brück *et al.,* 2007). The magnitudes of the magnetic entropy and the adiabatic temperature changes are strongly dependent upon the magnetic order process: the magnitude is generally small in antiferromagnets, ferrimagnets and spin glass systems.

Currently, alloys of gadolinium found to produce 3 to 4 K per tesla of change in a magnetic field can be employed for magnetic refrigeration or power generation purposes. Recent study on materials that display a giant entropy change exhibited that Gd5(SixGe1 - x)4, La(FexSi1 - x)13Hx and MnFeP1 - xAsx alloys, for example, are some of the most promising substitutes for Gadolinium and its alloys (GdDy, GdTy). These materials are called giant magnetocaloric effect materials (GMCE). Gadolinium and its alloys are the best material presented currently for magnetic refrigeration near room temperature since they experience second-order phase transitions with less magnetic or thermal hysteresis involved (Gomez *et al.,* 2013).

2.7 Electronic wave functions method

In DFT formalisms, the wave functions are fundamentals that are used to describe the probability of the electron in terms of position (x, y, z), time, t and momentum p. Using wavefunction, the probability of locating an electron within a given locality can be determined.

2.7.1 Schrödinger equation

Schrödinger equation can be used to show both physical existence of quantum particles and wave function, thus the name wave-particle duality arises. The many-body wave function $\psi($ r_i, $\{R\}R_A$)), is used to describe its quantum state through simulation of a system composed of N and M interacting electrons and ions respectively. The wave function ψ bank on the nuclear coordinates $\{R_A\}$ and the electronic coordinates. It is the answer to the Schrödinger time-independent equation. The non-relativistic form of this equation is given in equation 2.17.

$$\hat{H}\psi = \hat{E}\,\psi \qquad\qquad 2.17$$

With respect to equation 2.17,

The Hamiltonian can be written as in equation 2.18.

$$\hat{H} = \hat{T}e + \hat{T}_A + \tilde{V}_{Ae} + \tilde{V}_{ee} + \tilde{V}_{AA} \qquad\qquad 2.18$$

Where T is the kinetic energy operator and V is the potential energy operator.

The Schrödinger equation can be written as in equation 2.19.

$$[-\sum_i^N \frac{h^2 \nabla_i^2}{2e} - \sum_{A=1}^M \frac{h^2 \nabla_A^2}{2A} = -\sum_{i=1}^N \sum_{A=1}^M \frac{e^2 z_A}{|r_i - R_A|} + \sum_{i=1}^N \sum_{j>1}^M \frac{e^2}{|r_i - r_j|} + \sum_{A=1}^N \sum_{B>A}^N$$

$$\frac{e^2}{|R_A - R_B|}]\psi = E\psi \qquad\qquad 2.19$$

2.7.2 Born-Oppenheimer approximation

In most cases, the properties of solid state are determined by looking at the interplay of the electron's valence with comparatively slow-moving core atomic ions, and therefore the interplay of valence electrons within themselves. Owing to a large discrepancy of mass comparison between electrons and nucleus, the nucleus is approximately said to be eighteen hundred and thirty (~1830) times heavier than mass of an electron. As a result, kinetic energy of the nuclear is usually neglected when solving electronic problems. This is because kinetic energy of an electron is larger than kinetic energy of the nucleus hence usually treated as negligible.

The answer to the dynamics of electron difficulties during a frozen nuclear configuration is sorted out by separation of kinetic energy of the electron and that of ions. The total wave function equation can be written as in equations 2.20 and 2.21.

$$\psi[\{r_i\} - \{R_A\}] = \psi(\{r_i\} \times \psi \{R_A\}]) \qquad 2.20$$

$$H_e\psi(\{r_i\} = E_e\,\psi(\{r_i\} \qquad 2.21$$

When a Slater Determinant obeying Pauli exclusion principle with antisymmetric property is introduced in an electron system, this helps to overcome the difficulty encountered in solving equations 2.20 and 2.21. The wave function ψ is not observable, and $|\psi(X_1X_2\ldots\ldots X_N|^2\,dX_1,\,dX_{2\ldots}\ldots dX_N$ gives the possibility of locating an electron in a given dimension in the space $dX_1dX_2\ldots dX_N$. The anti-symmetry is obeyed that is, the exchange of two electrons changes only the sign of the wave function since the electrons are identical. The wave function can be written as in equation 2.22.

$$\psi(X_1X_2\ldots X_N) = -\psi(X_1X_2\ldots X_N) \qquad 2.22$$

The most important feature here is that the probability remains to be the same and can be given as in equation 2.23:

$$|\psi(X_1X_2\ldots X_N|^2 = |\psi(X_1X_2\ldots X_N|^2 \qquad 2.23$$

2.7.3 One-electron approximation

A single electron is considered in this case. The matrix determinant properties determine the nature of the Slater determinant which must obey the anti-symmetric property. Thus, particular single electron position dictates the nature of the electron wave function. Suppose the electron interaction is constant in a system, then Hamiltonian can be treated as the summation of energy due to each independent single particle in the system.

The difficulty of dealing with many-body system problem is simplified since the problem is narrowed down to minimise the accuracy of the one electron wave functions. The energy and many other properties can be obtained as soon as all solutions to the problem have been computed. When all the solutions are computed in the body system, the effective energy of the one electron system is written as in equation 2.24:

$$\hat{H} = \hat{T} + \tilde{V}_{ne} + \tilde{V}_{ee} = + \; \sum_i^N \frac{1}{2}\nabla_i^2 + \sum_i^N v(r_i) + \sum_{i<j}^N \frac{1}{ri} \qquad 2.24$$

2.7.4 Hartree Approximation

Born-Oppenheimer approximation significantly reduces the complexity of the Schrödinger equation but the resulting electronic Schrödinger equation is still enormously complex, due to the electron-electron interactions. It is possible to use wave functions which explicitly comprise inter-electronic distance, but this approach is computationally impracticable for all but the smallest systems. A more sufficient solution is to introduce the molecular orbital approximation, the simplest of which is the independent-particle, or Hartree, approximation wherein the total wave function is approximated by a product of orthonormal molecular orbitals (MOs). This idea closely follows the chemists' view of electrons occupying orbitals. The Hartree approximation assumes that each electron moves independently within its orbital and sees only the average field generated by all the other electrons.

2.7.5 Hartree-Fock Approximation (HF)

When dealing with many-body problems, difficulty is faced due to the interaction of particles in the system. The solution consisting of N body wave function and establishment of energy of the system remains to be a problem. Hartree-Fock (HF) found a solution by working on the energy of every electron in the mean static field. The Hamiltonian Fock equation can be written as in equation 2.25:

$$f_i = -\frac{\nabla_i^2}{2} - \sum_k^{Core} \frac{z_k}{r_{ik}} + V_i^{HF} \qquad\qquad 2.25$$

The HF has higher energy than the total energy because the HF method does away with the dynamic correlation in the system between the electronic movements in a material. Hartree method has an advantage because it utilises ideas of self-consistency and the self-consistent field when working out the solution of the large collection systems. A pair of electrons consists of an electron-electron which only communicates to another pair of electrons. In this way, electron of the many bodies wave function is considered to be independent and they communicate only through average field coulomb potential. The potential V(r) arises from both the nuclear electron interaction and the mean field obtained from the N-1 other electrons in one electron Schrödinger equation. Despite the Hartree equations utilising the concept of self-consistent field methods, its approximation fails to obey the Pauli exclusion principle. The principles require that the wave of the many-body function be antisymmetric whenever the interchange of any two electron positions occurs. This

odd function exchange manifests itself during the formation of a slater determinant of a one particle orbitals (Cenni, 1991).

2.8 Density Functional Theory (DFT)

It has been reported that the DFT formalism is unable to reproduce a realistic electronic structure, as it fails to open the bandgap (Yablonovitch *et al.*, 1991) or underestimates it. The density functional theory does not use the N-body wave functions of the electrons, but the total density of electrons (Terakura *et al.,* 1984). The electron density is a physical characteristic. When the number of electrons increases, it is easier to be calculated. More importantly, shows that DFT overcomes the principal disadvantage of the Hartree-Fock method, which abandons the electron correlation (Fleig, 2012). Hence, DFT improves the calculation accuracy significantly, whereas the exchange part in HF is defined exactly.

Hohenberg and Kohn (1964) came up with two theorems, first theorem of DFT consists of external potential $\tilde{V}_{et}$ ($\bar{r}$) to the system which arises from nuclei and is a distinct function of the electronic density ρ ($\bar{r}$) (Anisimov *et al.*, 1991). The second theorem of DFT takes care of the functional F_H [ρ] that gives the lowest energy i.e., the lowest state energy of the system in the case of the input density being the actual density of the ground state. The two theorems are substituted with three coordinates s (n (x; y; z)) with a single function doing away with a large number of variables in HF function (Hohenberg & Kohn, 1964). Also, the functional can be described accurately as a function of a function with a probability of finding first electron in dx_1, the second electron in dx_2, N electron in dx_N can be written as in equation 2.26.

$$| \psi(X_1 X_2 ... X_N |^2 \quad dx_1 \, dx_2 ... dx_N \qquad\qquad 2.26$$

The probability of finding electrons in a volume element of one dx_1 while the other electron anywhere is obtained by integrating over space a spin co-ordinate of electron 2,3…N and the spin coordinate of first electron as can written as equation 2.27.

$$((\int \cdot \cdots \int \Psi |x_1 x_2 \cdots x_N| \, dx_1 \, dx_2 ... dx_N) \, dr_1) \qquad\qquad 2.27$$

The probability of finding the first electron is obtained through multiplication with dr_1 as shown in equations 2.28 and 2.29.

$$N ((\int \cdots \int \Psi |x_1 x_2 ... x_N|^2 \, dx_1 \, dx_2 ... dx_N) \, p_{(r)} dr_1) \qquad\qquad 2.28$$

$$N ((\int \cdots \int \Psi |x_1 x_2 ... x_N|^2 \quad dx_{s1} dx_2 ... dx_N) \, p_{(r)} dr_1) \qquad\qquad 2.29$$

2.8.1 The Hohenberg Kohn Theorem (H-K)

Hohenberg and Kohn (1964) actualised the application of DFT by coming up with a simple first theorem involving N interacting particles in a system. Using the first theorem, H-K discovered that in an external field potential ($V_{ext(r)}$ for a system of N interacting particles, $V_{ext(r)}$ is a distinct and unique functional of the density. Taking into consideration that the ground state is non-degenerate and considering the variational principle which champions that no wave function can yield an energy that is less than the energy of $V_{ext(r)}$ for $\hat{H}_{ext(\sim r)}$. Therefore, the H-K theorem concludes that the charge density in the ground-state gives energy of the ground-state (E_0). The universal functional of the charge density n(r) is given by $F_{[n(r)]}$ which is treated as external energy. This way, DFT reduces this system with the N-body problem to a solution of just only three-dimensional function n(r) which minimises a functional $E_{[N(r)]}$. In many cases, a ρ(r) is trial density (Dreizler & Gross, 1983), which must meet boundary conditions; ρ(r)≥0 and equation 2.30.

$$\int \rho(r)dr = N \qquad\qquad 2.30$$

The trial density ρ(r), usually has an association with some external potential V_{ext}. Therefore, an upper bound to the true ground state energy E_0 of a system is represented by the functional of F_{HK}. The Hamiltonian equation showing association of ρ(r) is written as in equation 2.31.

$$< \Psi|H|\Psi > = T[\rho]+[\tilde{V}_{ee}[\rho]+ \int\rho(r\,V)_{ext}dr' = E\,[\rho]>E_0(\rho_0) =< \Psi 0|H|\Psi 0 > \qquad 2.31$$

2.8.2 Kohn-Sham equation

The studies by Kohn and Sham (1964) show that substitution of an interactive system for a non-interactive system on the basis that electronic ground states are equal when solving Schrödinger equation. The universal density ρ(r) takes care of all total energy in the system. At the ground state, the energy is lowest which gives the fundamental state $\rho\,(\bar{r}) = \rho_0\,(\bar{r})$. The electron clouds have a total energy equation that can be written as in equation 2.32.

$$E[\rho] = T[\rho] + \tilde{V}_{ee}[\rho] + E_c\,[\rho] + \int \tilde{V}_{e\,t}\,(r)\rho(r)d^3_r \qquad 2.32$$

The DFT theory is the best theory among other theories since it is exact and has no any approximation. The only unknown term is $E_c\,[\rho]$, the exchange-correlation term. The total potential includes the external potential and the impacts of the Coulomb interaction between the electrons, i.e. the exchange and correlations interactions written as in equations 2.33 and 2.34.

with

$$V_{XC}(r) = \frac{\delta Exc[\rho]}{\delta \rho} \ , \ \rho_{(r)} = \Sigma_1 |\Psi_i(r)|^2 \qquad\qquad 2.33$$

and

$$\int \rho_{(r)} \, dr = N, \ \langle \Psi_i | \Psi_j \rangle = \delta_{ij} \qquad\qquad 2.34$$

2.9 Exchange-Correlation energy

The energy approximations function in density function theory is given by exchange-correlation which compose of general gradient approximation and local density approximation (Huang, 2018).

2.9.1 Generalized Gradient Approximation and Local Density Approximation

The Generalized Density Approximation (GGA) curb the shortcoming of the local density approximation (LDA) method by considering the body collection system as both a non-uniform electron gas and non-local electron effects in the functional (Perdew *et al.*, 1992, 1993). This is because GGA is constructed using data from LDA. The term having exchange-correlation term can be given as a function of ρ and ∇_ρ written as in equation 2.35.

$$E_e^{LDA} = \int \varepsilon[c(r)[\rho(r)] + \nabla \rho] \, d^3r \qquad\qquad 2.35$$

The GGA has several advantages over LDA since allows for a larger fluctuation (Hammer *et al.*, 1993). Furthermore, the GGA usually gives higher results than LDA, in terms of atomisation energies, total energies, structural energy differences, and energy (Burke *et al.*, 1995, 1998). The Perdew Burke Ernzerhof is a more advanced version of a gradient-corrected GGA functional (Stixrude *et al.*, 1994). The Perdew Burke Ernzerhof is characterised by all parameters having fundamental constants of simple derivation. The functional is used to solve the problem involving both solids i.e., metals and molecules (Perdew *et al.*, 2008; Vosko *et al.*, 1980).

2.10 Pseudopotential

Calculations in the Quantum Espresso software are performed using the plane wave basis set. The basis set takes care of free electrons in a system intending to reproduce local features of a particular material in terms of regions and bonds where there are rapid wavefunction oscillations for example around the nuclei. The substitution of real potential with pseudopotentials which gives easy treatment and introduction of frozen core which it composes of core and valence electrons. The wavefunction is imitated by a soft wiggle pseudo-wavefunction with the same charge as the all-electron wavefunction within this region (Hamann *et al.*, 1979). Therefore, the valence

electrons determine most properties of materials such as electronic, structural and mechanical properties. *Ab initio* approximation pseudopotentials are most preferred to the full approximation potential method since it considers solemnly mobile valence electrons leaving the deep inner core states and also the sturdy potential binding them to the nuclei creating the calculation comparatively easier. The ion cores usually play a minimal role in a material system, nevertheless, their well integration into pseudo potentials plays a crucial role in the plane wave basis sets in electronic structures calculation. The real potential and pseudo-wave function both converge at a similar potential at the point called a certain cut-off radius, r_c (Blanc *et al.,* 2019).

In the Schrödinger equation, Coulomb's potential is taken care of by an effective potential term, in order to cater for problems created by motions of ion core, it is by use of Pseudopotentials. The Pseudopotentials function is to imitate the character of an atom ion core. This results in the elimination of core states with pseudo-wave functions with fewer peaks describing the valence electrons. Blöchl (1994) showed that Projector augmented wave (PAW) pseudo-potential (PP) is a way for reformulating standard Kohn-Sham formalism with numerically inconvenient behaviour into a more computationally digested type, that involves a unique Kohn-Sham formalism problem with certain corrections. In the projector augmented wave (PAW) pseudo-potential (PP), the core electrons are considered frozen at the atomic solutions and therefore regarded as the full all-electron wavefunction (Kulińska *et al.*, 2006). It is a distinctive method of determining the electron structure of alloys and materials since it describes well the nodal peak behaviour of valence electrons plane wave function and at an identical time allows the inclusion of the higher core states into the self-consistent interaction procedures.

Studies by Andersen (1975) report that Projector augmented wave (PAW) pseudo-potential (PP) derives concepts from the all-electron linear augmented plane wave (LAPW) methodology. It is a generalisation of those PP and LAPW methods and allows for DFT calculations to be conducted with greater computational efficiency. During this study, norm-conserving pseudo-potentials are used to mimic the inner core electrons and also nuclei. In the USPP methodology, the charge of the core electrons is allowed to change, whose variation is compensated with the introduction of localised atom-centred augmentation charges (Vanderbilt, 1990).

2.10.1 Pseudopotential basis sets

The pseudopotential theory also aims at scaling down the complexness of the calculations. Therefore, the valence electrons are the one that plays a significant role in the physical and

chemical properties of a solid while the core electrons play a minimal role. The pseudopotential eliminates core electrons and strong attractive nuclear potential and imitates them through substitution with a weaker effective core potential. The imitation step up as a set of pseudo wave function instead of an actual valence wave function (Hamann *et al.*, 1979). By doing so, calculations became simplified. The valence electrons are written as pseudo-functions and can be shown in Figure 2.6 (Payne *et al.*, 1992).
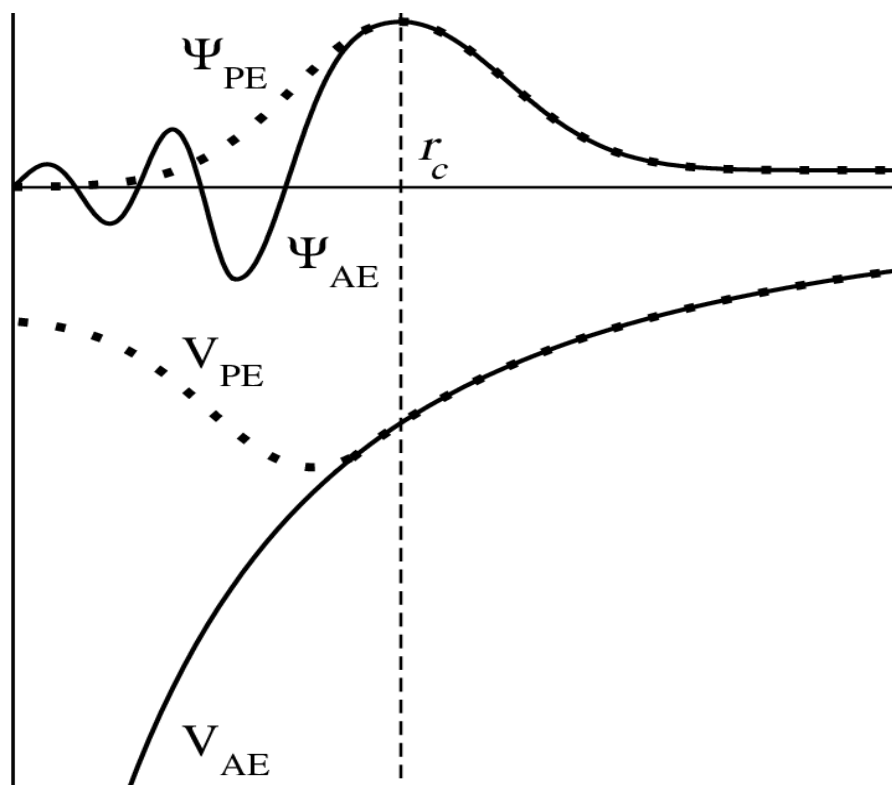
Figure 2. 6: The pseudo-electron (PE) (dotted lines) and all-electron (AE) (solid lines) wave function, Ψ, and potential, V. The PE and AE values must match at r ≥ rc where rc represents the core radius

Source: Payne et al. (1992).

There are $\boldsymbol{\Psi}^{AE}$ various types of pseudopotentials available, for example, projected augmented waves (PAW) method, ultra-soft pseudopotentials (USSP), and norm-conserving pseudopotentials (NCPP). The goodness of the USSP and PAW schemes is that small numbers of plane waves are needed to reach convergence. In the USPP methodology, the charge of the core electrons is allowed to change, whose variation is compensated with the introduction of localised atom-centred augmentation charges (Vanderbilt, 1990). The Projector Augmented Waves (PAW) method will

be key in our calculations. Blöch came up with the augmented plane wave method and implemented it into the VASP software by Kresse and Joubert (1999). The wave function of all the electrons in the PAW method is written as in equation 2.36.

$$| \boldsymbol{\Psi}^{\mathbf{AE}} \rangle = | \boldsymbol{\Psi}_v{}^{\mathbf{PS}} \rangle + \Sigma_i c_i (| \boldsymbol{\Psi}_I{}^{\mathbf{AE}} \rangle - | \boldsymbol{\Psi}_I{}^{\mathbf{PS}} \rangle)$$ 2.36

where $\boldsymbol{\Psi}_v{}^{\mathbf{PS}}$ is the pseudo-function.

The equation of the $\boldsymbol{\Psi}_v{}^{\mathbf{PS}}$ is given as in equation 2.37.

$$\Psi_v{}^{PS} = \sum \langle \rho_I | \boldsymbol{\Psi}_v{}^{PS} \rangle \boldsymbol{\Psi}_v{}^{PS}$$ 2.37

Therefore, the wave function of all electrons can be written as in equation 2.38.

$$|\Psi\,\mathbf{AE}\rangle = |\Psi\,v\,\mathbf{PS}\rangle - \Sigma_i |\Psi\,I\,\mathbf{PS}\rangle\langle \rho\,I | \Psi\,v\,\mathbf{PS} \rangle + \Sigma_i |\rho\,i | \Psi\,v\,\mathbf{PS}\rangle\langle \rho\,i | \Psi\,v\,\mathbf{AE} \rangle$$ 2.38

The PAW pseudopotentials keep these forms for all the electrons.

2.11 Plane wave functions and Brillouin zone sampling

Plane waves are mathematical functional that give easy treatment mapping use as a fundamental description of the electronic plane wave functions of periodic systems. While Bloch's theorem stated that, in a body of the periodic system, each electronic plane wave function can be written as a multiplication of a periodic function. Therefore, the periodicity of a unit cell of atoms in three directions is modelled based on the periodic boundary conditions (PBC). The modelling of a stable system is achieved through the convergence of the total forces and energy. The plane wave basis sets are used to execute and expressed electronic density. According to Payne *et al.* (1992), Bloch's theorem is written as in equation 2.39.

$$\psi_{k\,(R+T)} = e^{ik.r}\,\psi_{k\,(R)}$$ 2.39

A finite solid mostly contains continuous quantum numbers. In the finite solid, a kinetic cut-off energy is used to limit the set to a sphere in the reciprocal space in use as shown in equation 2.40.

$$\text{Ecut-off} > \frac{h^2\,|K+T|^2}{2}$$ 2.40

The Brillouin zone which contains an infinite number of k-points is usually expressed in terms of Bloch's functions. There are several methods aimed at providing good choices of k-points such as the improved tetrahedron method (Blöchl *et al.*, 1994) which breaks up the cell in the reciprocal space into tetrahedra as well as the Monkhorst and Pack method that yield the generation a set of special points in the Brillouin zone (Monkhorst & Pack, 1976) generating a set of special points in the Brillouin zone. The equation of Bloch function $\psi_{I,R}$ is of great importance in finding the

solution of each k-point. The band energy is usually integrated over each k point in order to obtain total energy which can be written as in equation 2.41.

$$E = \sum \frac{1}{\Omega_{BZ}} \int E_{ik} \, g_i(k)dk \qquad\qquad 2.41$$

The volume of the Brillouin zone is given by Ω_{BZ} and the electronic occupation is represented by g_i of state i at point k.

2.12 Many-body interaction

The exchange-correlation functional usually exists as an approximation of the many-body effects due to the absence of self-energy contribution in DFT. The exchange-correlation functionals are described as median, the electron-electron interaction. The explicit treatment of the interactions between individual particles would lead to a degree of an impractical system of equations. Self-energy is a contribution of a small part of the energy of a particle in a system that relies on the mutual interaction of particles present in the whole system. This method gives us the advantage of working on properties of a material under study with maximum utilisation of computational resources with precision on accuracy and cost, hence anomalous results can be avoided. The HF method gives a calculation of self-energy for the ground state properties. Even though this method utilises greater computational cost, it gives higher accurate precision of different effects. Therefore, we can say that *ab initio* studies of the properties of material provide for the solution of quantum many-body systems involving electron coordinates and atomic interaction problems (Wilson, 1997).

CHAPTER THREE

MATERIALS AND METHODS

3.1 Introduction

Different methods were outlined to achieve the goals that were described in the previous section. The explanation of the properties and behaviours of many-body systems in physics, chemistry, material sciences, solid-state physics and quantum mechanics has played a significant role. This research work has been made possible through some approximate theoretical approaches such as first principle calculations. The first principle (*ab-initio*) calculations are theoretical approaches that depend on conventional fundamental laws of physics and do not depend on experimental models and fitting parameters as input sources.

In this research work, DFT formalism was the *ab-initio* approach that was used along with the plane wave pseudopotentials, and the projected augmented wave (PAW) within the GGA exchange-correlation to describe the electronic structure and investigate other properties of the proposed structures using the QE code (Giannozzi *et al*., 2009, 2017).

3.2 Computational details

Electronic structure calculations were performed using the full charge and spin-self-consistent method (Roy *et al.,* 2016; Ou *et al*., 2013). $FeMnP_{0.67} Si_{0.33}$ has a hexagonal structure (space group $P\bar{6}2m$, No. 189) with the low-temperature lattice parameters (Ma *et al.,* 2017; Pecharsky & Gschneidner, 1997) a = 5.866 a.u, c = 3.456 a.u.

The atomic positions used in this wok were generated from xcrysden software during input file creation. (Giannozzi *et al.,* 2009) and the radii of 2.4 a.u. (Fe) and 1.7 a.u. (P) were accounted for by ultra-soft pseudopotentials (Vanderbilt, 1990). The spin polarisation approach was applied to investigate the magnetic moment of the system as a model of both paramagnetic and ferromagnetic states.

Similarly, to the electronic structure, the magnetic moment orientation can be seen as similar to that of a $FeMnP_{1-x}A_x$ alloy, where atoms Fe_1 and Fe_2 keep opposite magnetic moments in an antiferromagnetic state and the same magnetic moment in a ferromagnetic state. In quantum espresso, both Fe_1 and Fe_2 atoms occupy the same crystallographic site, thus for x = 0.33, the total magnetic moment is zero (if the A_1 and A_2 magnetic moments have the same magnitude). In the case of two nonequivalent iron sublattices in $FeMnP_{0.67} Si_{0.33}$, this means that the 3f site atom is

for $Fe_1\uparrow(3f)$ and $Fe_2\downarrow(3f)$ and similarly for the 3g site, $Fe_1\uparrow(3g)$ and $Fe_2\downarrow(3g)$. The local μFe_1 and μFe_2 magnetic moments are non-zero and they are randomly distributed among the crystal sites, as for a ferromagnetic material above T_c. The spin polarisation calculations are post-processing which follows after scf and band structure calculations but starting magnetisation of atoms Fe_1 and Fe_2 was set at scf calculation after relaxation, subsequently the magnetic properties.

As predictable, the final magnetic moments in the AFM state were different from those obtained in the ferromagnetic state, since the electronic structure of a magnetic and non-magnetic system is different. Also, because of the two non-equivalent iron sites occupied in Fe by 'magnetic' atoms. For a fully converged crystal system, total and site-decomposed spin-dependent densities of states (DOS) were computed, using the spin-polarization approach technique of integration in the reciprocal space (Wang & Ye, 2003). The total and local magnetic moments were also calculated. The Fermi level (E_F) was determined using the generalised Lloyd formula (Mao *et al.*, 2013). Much of the information like Fermi energy, and total and absolute magnetisation was obtained from the output file after every step of the calculation.

3.3 Structural optimisation

Structural parameters for $FeMnP_{1-x}A_x$ (A_x= Si, Sn, Se and In) alloys optimisation were achieved through relaxing the atoms in *x*, *y* and *z* dimensions until the systems attained the lowest energy positions as per the set criterion for convergence. The atomic dimension in the relax positions was used to ensure both the k-point grid and the plane wave kinetic energy cut-off optimisation were achieved. The lowest energy of the system formed the basis of total minimum energy as a function of the cell volume. The lowest energy is due to the k-points and plane wave kinetic cut-off energy having augmented values. The variable cell relaxation algorithm was employed for obtaining the minimised total energy value by using ultra-soft pseudopotentials and Perdew-Burke-Ernzerhof (PBE) exchange-correlation functions. For each step, the ionic positions and the lattice parameters were optimised with energy and force convergence criteria of 10^{-5} eV/atom and 0.005 eV/A respectively.

In this study, the special k-points were generated automatically using the Monkhorst-Pack scheme (Roy *et al.*, 2016). Monkhorst-Pack scheme ensures that the irreducible part of the Brillouin Zone (IBZ) is integrated over a mesh of uniformly spaced 3 3 5 k-points. Following a rigorous optimisation process, the k-points grid was varied over a wide range of values (2x2x3 to

8x8x15) since transition metals like iron are known to require large k-point grids. The kinetic cut-off energy of 96 Ry was used with a charge density of 720 Ry.

3.3.1 K-points optimisation

The k-points optimisation was done using the lattice parameter empirical value. The energy unit for kinetic Energy cut-off was set in Rydberg for $FeMnP_{1-x}A_x$ (A_x=Si, Se, Sn, In) alloys. The generation of special k-mesh points was achieved using the Monkhorst-pack scheme which enables the integration parts of the irreducible Brillouin zone (IBZ) mesh from a small size to a dense large size since $FeMnP_{1-x}A_x$ (A_x = Si, Se, Sn, In) alloys were heavy grid.

All calculations were performed for collinear spins without spin-orbit coupling. The optimisation of atomic positions was carried through the Broyden, Fletcher-Goldfarb-Shanno (BFGS) algorithm where the forces and energy minimisation processes are considered during structural relaxation (Broyden, 1970). The host compound, $FeMnP_{0.67}Si_{0.33}$ as well as the doped compounds were optimised making sure that the minimum energy was achieved. This ensured that all the compounds were at their most stable state before investigation of the properties.

3.3.2 Optimisation of plane wave kinetic cut-off energy

The k-point grid convergence is accustomed to calculating the plane wave cutoff energies. During the study on plane wave cut-off energy, the lattice parameters and k-points mesh were set at their optimised values in the entire calculations. For every step, the kinetic cut-off energy was varied under constant lattice parameters and force convergence criteria of 10^{-5} eV/atom until optimisation was achieved.

To find the actual energy cut-off and k-point mesh, the self-consistent field (SCF) convergence test was performed for all parameters. Scf convergency was achieved at a convergence threshold of 10^{-6} Ry. The kinetic energy cut-off of 96 Ry and a charge density of 720 Ry were applied, for expanding the plain wave functions and a $3 \times 3 \times 5$ k-point mesh for the Brillouin zone (BZ) integration (Pack & Monkhorst, 1977).

3.3.3 Structural optimisation.

Structural optimisation was done for $FeMnP_{0.67}Si_{0.33}$, followed by the substitution of Si with Se, In and Sn at substitutional sites of the host compound. Structural relaxation was done after the introduction of each new element in the alloy using Broyden, Fletcher, Goldfarb and Shannon (BFGS) (Broyden, 1970). BFGS attempts to solve a general nonlinear optimisation problem with

no constraints. Considering the two magnetic arrangements, that is FM and AFM, k-point meshes of 3×3×5 and 5×5×3 were utilised respectively to obtain the most energetic stable states. The FM state had 9 atoms per cell while the AFM state a supercell of 1×1×2 with 18 atoms was considered.

3.4 Electronic properties optimisation

In materials, there is the formation of very close discrete energy levels characterised by continuous bands. To study the bands, the Density of state (DOS) calculations were done to obtain the graphs. This was crucial in analysing the energy bands which brings out the number of state occupations by electron available in a unit cell at a given energy. The DOS contains vital information concerning the site-projected DOS (PDOS) as well as the spin-up (α) and spin-down (β) electronic states. Therefore, without the knowledge of bands using the PDOS chemical bonds would not be studied. Modifications in their intensity and position indicate charge transfers as well as ionic or covalent interactions. The gnuplot and Xmgrace were used to plot the band structure and PDOS graphs.

3.5 Magnetic optimisation

The magnetic properties of a material can be understood from the electronics and PDOS properties of the material. Starting magnetisation is presented in the input file to determine the magnetic properties of the compound under study. During magnetic optimisation, starting magnetisation of 0.2 Bohr magneton was introduced. It was varied from 0.2 μ_B to 1 μ_B in the range of 0.2 μ_B and respective total energies were also recorded.

Starting magnetisation of 1 Bohr mag. was introduced on Fe during calculations since it was bearing minimum energy during optimization of starting magnetisation. For the case of FM, starting magnetisation of 1 was introduced on the Fe atom for a spin-up polarisation while +1 and -1 were both set for the spin-up and spin down respectively in the case of AFM phase. This was done after the optimisation of starting magnetisation referenced in Table 4.1.

3.6 Magnetic properties

DFT calculations in this work were performed using a plane-wave basis set method with GGA parameterised by Perdew-Burkew-Enzerhof (PBE) exchange-correlation methods (Kohn & Mattsson, 1998) as instigated in the QE simulation package (Giannozzi *et al.*, 2017). In the calculation of bond energies, PBE is among the most popular functionals because it has been

known to significantly reduce the mean absolute error to the nearly desired chemical accuracy higher than 1 kcal/mol or 50 meV/atom (Makov & Payne, 1995). It was chosen in this study because its construction ensures that it retains some physical features in both the correlation and exchange parts.

Ultrasoft pseudopotentials were used for the compound examined in this study. All the pseudopotentials utilised in this work were generated by Giannozzi *et al*. (2009). After full optimisation of the structure, band structure calculation was performed, thereafter, DOS and PDOS were involved in calculations as post-processing to extract the parameters of materials. Similarly, a spin-polarised approach for PDOS was implemented within the calculations to determine the magnetic properties of the system. The moments of the atoms within the same unit cell remain constant and an alternating arrangement of spin-up and spin-down moments were used along the *z*-direction.

From the output files generated by SCF calculations, both total magnetisation and absolute magnetisation per cell were obtained, referenced in Table 4.2. We have chosen $FeMnP_{0.67}Si_{0.33}$ stoichiometry for the calculations with a 1: 1 and 2: 1 ratio for the nonmetallic and metallic atoms, respectively, to distinguish the crystallographic sites with the chemical species (Ma *et al.,* 2017). The system with a high number of total magnetisations per cell with no change in the structure during phase transition is considered the best candidate for the magnetic refrigerant. The charge density difference was determined for the system after substitution was calculated.

CHAPTER FOUR

RESULTS AND DISCUSSION

4.1 Introduction

To comprehend the magnetic properties calculated in this work, the electronic band structure and PDOS were factors to consider. A table of starting magnetisation as a function of total energy was computed to distinguish the optimal starting magnetisation. The results are recorded in Table 4.1, where energy differences were also calculated which is the variance between the minimum energy and the other calculated energy values. This was done by varying starting magnetisation from $0.2\mu_B$ to $1.0\mu_B$ and respective total energies were obtained after calculations as recorded in table 4.1. From the table, it is clear that starting magnetisation of $1.0\mu_B$ was the most stable state of the compound bearing a minimum energy of -1425.57280534 Ry. Energy difference was calculated by subtracting the most minimum energy in column two from each total energy in column two to obtain the energy difference in column three.

Table 4.1: Starting magnetisation and total energy

Starting magnetisation μ_B	Total energy in Ry	Energy difference (Ry)
0.2	-1425.57280514	0.00000020
0.4	-1425.57280522	0.00000012
0.5	-1425.57280482	0.00000052
0.6	-1425.57280149	0.00000385
0.8	-1425.57280325	0.00000209
1.0	-1425.57280534	0.00000000

The optimized parameters used in the study were 3 by 3 by 5 k-points, kinetic energy cut off of 96 Ry, charge density of 720 Ry and crystal parameters of **a=b** =5.811 a.u and **c** = 3.4296 a.u The two spin channels are symmetric for the AFM state of all of the compounds, indicating the disappearance of the overall magnetic moment of the AFM cell. From the overall results, because of the breaking symmetry, several bands split and new states appear close to the Fermi level as the compounds undergo the FM to AFM transition (Xu *et al.,* 2017). This is shown in AFM band structures. The band structure showed that the materials studied were all metallic since CB and VB overlapped (Liu et al., 2017; Modak *et al.*, 2015; Mulwa, 2012).

4.2 Doping FeMnP with Si

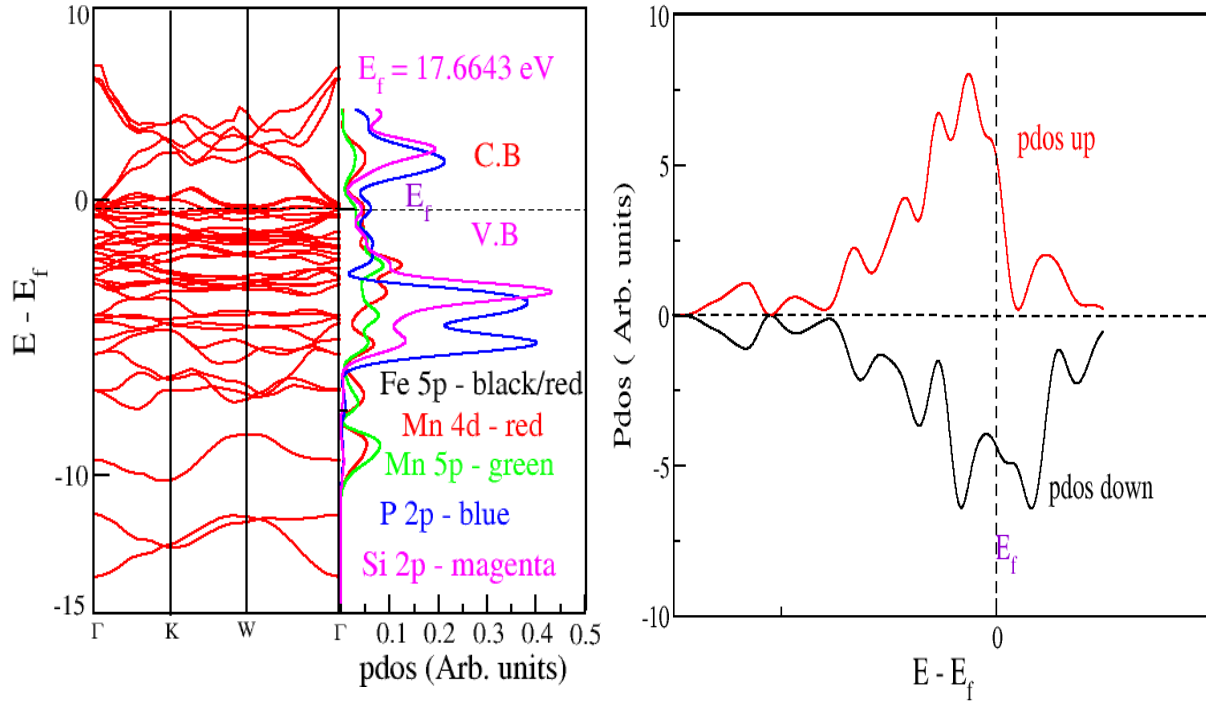### 4.2.1 Base structure FeMnP$_{0.67}$Si$_{0.33}$ electronic and spin polarisation analysis

FeMnPSi alloy was treated as the base compound in this entire study. Its electronic and magnetic properties were investigated under two magnetic phases, that is, ferromagnetic and antiferromagnetic phases.

4.2.2 Ferromagnetic phase of FeMnP$_{0.67}$ Si$_{0.33}$

Figure 4.1a is an illustration of the band structure of FM for the base FeMnP$_{0.67}$ Si$_{0.33}$ alloy and Figure 4.1b shows the total PDOS spin polarisation graph of the base FeMnP$_{0.67}$ Si$_{0.33}$ alloy. Figure 4.1a is a representation of band structure in the FM phase of FeMnP$_{0.67}$Si$_{0.33}$ through the path Γ-K – W – Γ, generated from the xcrysden tool. In the figure, the Fermi level (E$_f$) lies on VB, and VB is observed to be overlapping with CB indicating the metallic nature of the system (Bazine *et al.,* 2019). In the approximation of local magnetic moment with the phase transition, the PDOS graphs were plotted. In Figure 4.1b, the spin polarisation graph indicated a non-symmetrical graph between total PDOS up and total PDOS down thus showing the presence of local magnetic moments hence magnetic in nature (Mulwa, 2012).

In Figure 4.1b spin-polarised graph indicated a non-symmetrical relationship between PDOS up and PDOS down thus some local magnetic moments in the compound are exhibited by the alloy. This is evidence of the magnetic nature of the material (Modak *et al*., 2015; Mulwa 2012). This observation was also in agreement with a study carried out by Bazine *et al.* (2019) who reported the presence of local magnet moment by evidence of a nonsymmetric relationship between pdos up and PDOS down. Similarly, in figure 4.1b, PDOS of FeMnP$_{0.67}$Si$_{0.33}$ attained from the spin-polarised calculations presented E$_f$ corresponding to the band structure graph in figure4.1a, that is the E$_f$ in figure 4.1a is observed to be at the same energy level as the E$_f$ in figure4.1b. The result displayed consistency in band structure since the valence and conduction bands meet at the E$_f$.

The non-symmetric nature of PDOS shown by a spin up and spin down exhibited the magnetic nature of FeMnP$_{0.67}$Si$_{0.33}$ alloy. The dotted lines in Figure 4.1a and Figure 4.1b signify the Fermi levels. From the band structure graph, it is practical that the valence band is conquered by 2p orbitals from silicon and 2p orbitals from phosphorus as they project at higher energy levels than the others.

a) Electronic band structure of ferromagnetic FeMnP$_{0.67}$Si$_{0.33}$

b). Spin polarisation graph of ferromagnetic FeMnP$_{0.67}$Si$_{0.33}$

Figure 4. 1: Electronic band structure and spin polarised graphs for FM FeMnP$_{0.67}$Si$_{0.33}$

4.2.3 Antiferromagnetic phase for FeMnP$_{0.67}$Si$_{0.33}$

The antiferromagnetic state of the material exhibited non-magnetic nature. This was demonstrated by Figure 4.2b and Table 4.2. Figure 4.2 is an illustration of the AFM states of FeMnP$_{0.67}$Si$_{0.33}$. From the band structure graph, E_f of the system is located on top of VB and no states are observed in CB. The spin polarisation graph shown in Figure 4.2b presents perfect symmetry of total PDOS up and down PDOS showing no magnetic local moment. This exhibits the nonmagnetic nature of the material. In this study, when comparing the total PDOS of FeMnP$_{0.67}$Si$_{0.33}$ in different magnetic states, it is clear that the FM state has larger PDOS at E_f than that of the AFM state, but the AFM state should have larger PDOS at Fermi level than FM (Ma *et al*., 2017). This is an indication of mechanical instability along phase transition (Liang & Whangbo, 1993; Womes *et al*.,1997).

Figure 4.1a, which is the band structure of the Antiferromagnetic phase of the FeMnP$_{0.67}$ Si$_{0.33}$, found through Γ – U – Γ points of high symmetry. In VB there is the existence of PDOS states in empty bands. This structure displayed unstable properties since PDOS are projected in empty bands. This may have resulted due to missing bonds during the transition (Liang & Whangbo, 1993; Womes *et al*.,1997). This is exhibited during the magnetic phase transition of the system from ferromagnetic to antiferromagnetic transition (Rakel *et al.,* 2008).

Compared to Figure 4.1a, in the FM phase of the same system, there was an overlapping of conduction and valence bands of the system, this is lost in the AFM phase where the E$_f$ shifts from the top of the VB to the top of the CB (Charif *et al.*, 2020). Figure 4.1b is a spin polarisation graph from the total PDOS of FeMnP$_{0.67}$ Si$_{0.33}$. There is a symmetric relationship between spin-up and spin-down total PDOS which implies the absence of local magnetic moments of the system thus exhibiting non-magnetic nature. Half of the atoms in the cell have a magnetisation that is opposite to the magnetisation of the remaining half of the atoms, therefore, the total magnetisation is zero and the spin-up and spin-down contributions are the same (Tripathy *et al.,* 2006).

a) Electronic band structure of antiferromagnetic FeMnP$_{0.67}$ Si$_{0.33}$

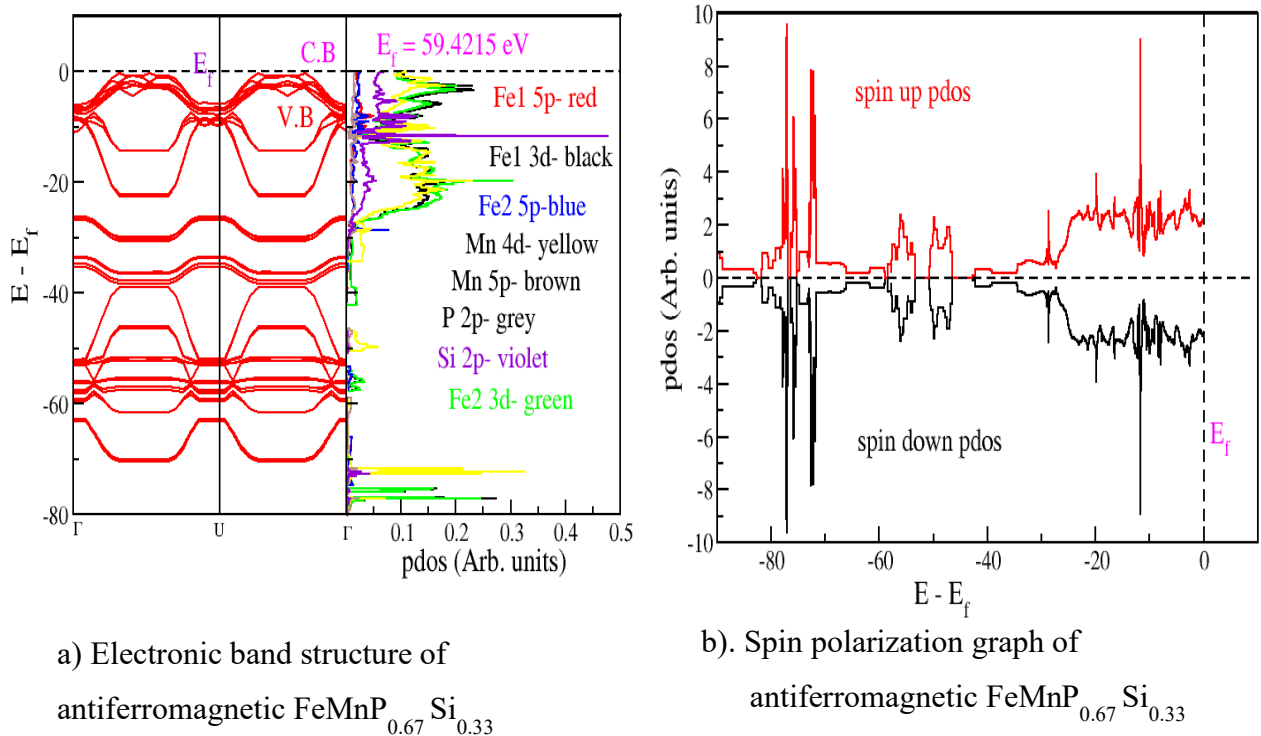b). Spin polarization graph of antiferromagnetic FeMnP$_{0.67}$ Si$_{0.33}$

Figure 4. 2: Electronic band structure and Spin polarization graph of AFM phase for FeMnP$_{0.67}$Si$_{0.33}$

4.3 Substitution of Si with In, Se and Sn.

The atoms of silicon in the parent compound FeMnPSi were later substituted with Se, In and Sn atoms. Their magnetic properties were investigated in both ferromagnetic and antiferromagnetic states just like the parent compound. The base structure was magnetic, and on substitution of Si atom in $FeMnP_{0.67}Si_{0.33}$ with Se, In, Sn atoms, there was a need to check whether the two phases were magnetic too. This was done by carrying out spin polarisation after substitution in both two magnetic phases, that is both FM and AFM. All FM states of the materials showed magnetic properties as this was confirmed by spin-polarisation graphs while AFM states showed perfect symmetry in their spin-polarised graph thus indicating non-magnetic properties (Bazine *et al.*,2019; Miao *et al.*, 2016; Modak *et al.*, 2015).

4.4 Ferromagnetic states of FeMnP-A (A=In, Se, Sn)

$FeMnP_{0.67}Si_{0.33}$ compound was optimised and the system properties were investigated in the FM phase. The results exhibited that the system is magnetic and thus can be used as a magnetic refrigerant. Comparing the total PDOS of $FeMnP_{0.67}Si_{0.33}$ in two different magnetic phases, it was realised that the FM phase has PDOS states in CB but no PDOS states at CB for AFM phase (Fig.4.1). From reported work, AFM phase should have more PDOS states in CB while the FM phase, should have few PDOS states in CB (Bazine *et al.*, 2019; Ma *et al.,* 2017). This is not the case in our base compound ($FeMnP_{0.67}Si_{0.33}$), therefore the need for substituting Si in the base compound, to achieve a stable refrigerant under magnetic phase transition.

The strongest moment ($\sim 2.2\mu_B$) was found on the Fe (3g) pyramidal site formed by 5P neighbours, whereas the Fe(3f) moment of the tetrahedral (3f) site formed by 4P neighbours is about four times smaller ($\sim 0.6\mu_B$) (Wiendlocha *et al.,* 2008). This site of the atoms is illustrated in Figure 2.1.

4.4.1 Ferromagnetic phase of $FeMnP_{0.67}In_{0.33}$

Figure 4.3a represents the band structure of the FM phase for $FeMnP_{0.67}In_{0.33}$ through the paths Γ- K – X – Γ. In this illustration, E_f is found on top of VB and there is also an overlapping of CB and VB presentation that the material possesses metallic properties. Large total PDOS is observed below E_f from Fe-3d states and Mn-4d states. The Fe and Mn atoms are magnetic giving evidence that Figure 4.3a denotes a magnetic phase. Comparing these results with observations from Figure

4.1a, it is understood that total PDOS is dominated by Si and P atoms which are non-magnetic atoms, which translates that the system possesses a low magnetic moment (Sturm *et al.,* 2017).

Figure 4.3b demonstrates the spin polarisation graph of $FeMnP_{0.67}In_{0.33}$ with non-symmetrical nature thus exhibiting magnetic properties. Total PDOS indicated the magnetic nature of $FeMnP_{0.66}In_{0.33}$ system and was quantified as 9.98 μ_B per cell as a total magnetic moment for the FM phase of the material. This value was attained from the SCF output file. From the spin polarisation figure, one spin population is larger than the other and the density of states (DOS) of the two spins is not aligned anymore in a symmetrical manner. To take a better understanding of magnetism, the total PDOS of the system was illustrated. In this case, the present calculations indicated that the system is ferromagnetic (FM). On the other hand, the net magnetic moment of isolated base reference $FeMnP_{0.67}Si_{0.33}$ is 9.81 μ_B per cell. From this, there was a significant increment in magnetic moment. This increment of the magnetic moment of $FeMnP_{0.67}In_{0.33}$ system can be said that it was due to the rearrangement of electronic charge of 4d and 3d orbitals of the Mn and Fe respectively (Charif *et al.,* 2020). Since the normal ground-state electronic structure of Mn atom has the [Ar]3d5 4s² configuration, the 4s shell is closed with two electrons and the exchange interaction favours as many electrons having the same spin orientation as possible ($3d^5$ Mn) (Charif *et al.*, 2020; Roy *et al.,* 2016).

The low-lying electrons $3S^23P^6$, which are considered valence electrons in the present calculations, are also filled and do not contribute to the magnetism of an isolated Mn atom (Dubrovin *et al.*, 2020). The reflection of the calculations showed that the increment of the magnetic moment in $FeMnP_{0.67}In_{0.33}$ is due to the transfer and spin rearrangement of charge at 3s, 4s and 3p orbitals of Mn atom. On substituting Si with In there was an increase in the magnetic moment per cell from 9.81 μ_B to 9.98 μ_B. This positive result showed that In could be the best substitute for Si in FeMnPSi magnetic refrigerants.
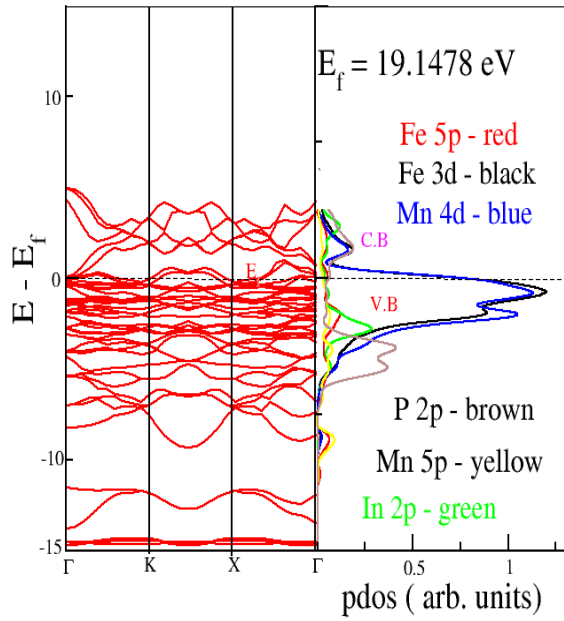
a) Electronoic band structure of ferromagnetic FeMnP$_{0.67}$In$_{0.33}$

b). Spin polarization graph of ferromagnetic FeMnP$_{0.67}$In$_{0.33}$

Figure 4. 3: Electronic band structure and spin polarization graphs for FM phase FeMnP$_{0.67}$In$_{0.33}$
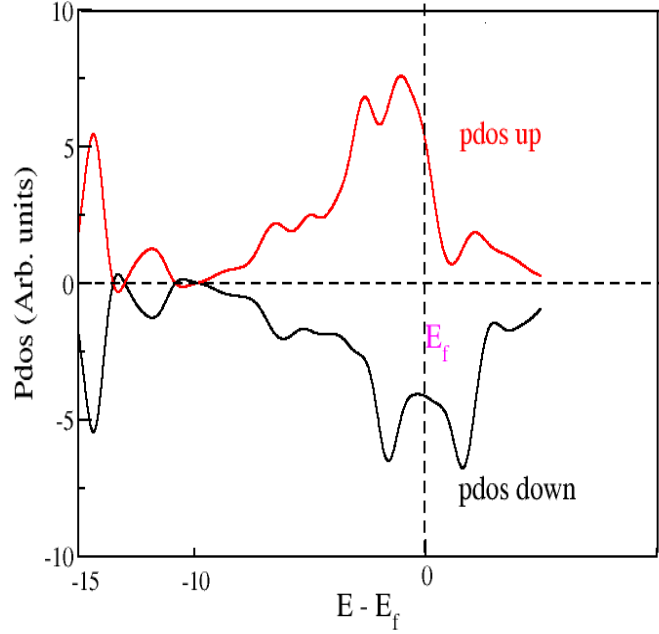
4.4.2 Ferromagnetic phase of FeMnP$_{0.67}$Se$_{0.33}$

Figure 4.4a shows the calculated band structure and total PDOS of FeMnP$_{0.67}$Se$_{0.33}$. The electronic band structure was attained along the high symmetry path $\Gamma - K - X - \Gamma$ as shown in Figure 4.4a. E_f is found on top of VB, there is also an overlapping of CB and VB indicating that the material possesses metallic properties. It is observed that below $E_{f,}$ that is in the VB, the PDOS is dominated by 4d orbitals from Mn and 3d orbitals from Fe atoms.

Figure 4.4b presents a spin polarisation graph with non-symmetrical nature which can be said that magnetic properties are exhibited by the material in this phase. Total PDOS indicated the magnetic nature of FeMnP$_{0.67}$Se$_{0.33}$ system and was quantified as 9.02μ_B per cell as a total magnetic moment for the FM phase. This shows that on substituting Si with Se, the magnetic moment per cell reduced from 9.81μ_B to 9.02μ_B. This is a clear justification that Se is not a suitable substitute for Si.

a) Electronic band structure of
ferromagnetic FeMnP$_{0.67}$Se$_{0.33}$

b). Spin polarization graph of
ferromagnetic FeMnP$_{0.67}$Se$_{0.33}$
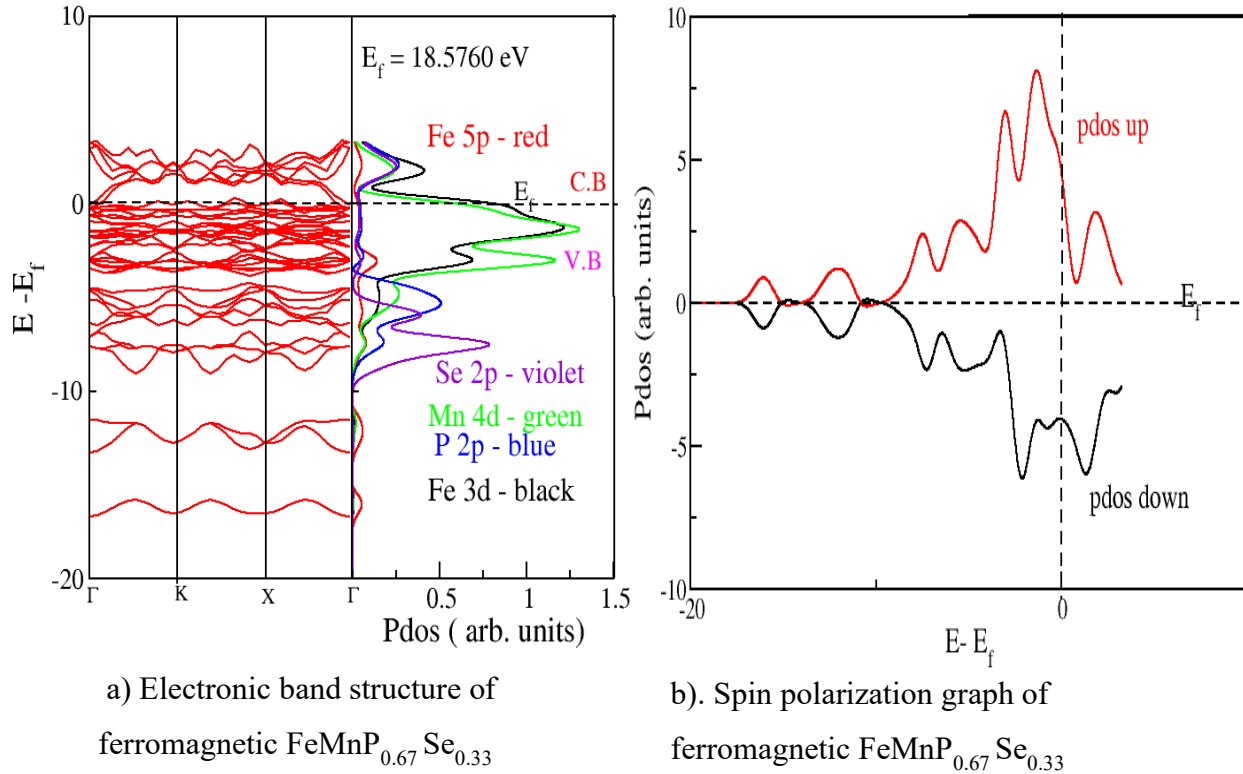
Figure 4. 4: Electronic band structure and spin polarization graphs for FM FeMnP$_{0.67}$Se$_{0.33}$

4.4.3 Ferromagnetic phase of FeMnP$_{0.67}$Sn$_{0.33}$

In Figure 4.5a, the calculated band structure and PDOS of FeMnP$_{0.67}$Sn$_{0.33}$ is illustrated. The electronic band structure was obtained along the high symmetry path $\Gamma – W – W – \Gamma$ as indicated in figure 4.4a where E$_f$ is located on top of VB, and also overlapping CB and VB showing that the material is metallic. It is observed that the 4d orbitals from Mn and 3d orbital from Fe atoms dominate the VB.

Figure 4.4b presents a spin polarisation graph of FeMnP$_{0.67}$Sn$_{0.33}$ with non-symmetrical nature between PDOS up and PDOS down. This is a demonstration of some local magnetic moments thus showing the magnetic nature of the material. Total PDOS indicates the magnetic nature of FeMnP$_{0.67}$Sn$_{0.33}$ system and is calculated as 9.64μ_B per cell as a total magnetic moment. This shows a reduction of magnetic moment per cell from 9.81μ_B to 9.64μ_B. This is a justification that Sn also cannot be a suitable replacement for Si.

a). Electronic band structure of ferromagnetic $FeMnP_{0.67}Sn_{0.33}$

b). Spin polarization graph of ferromagnetic $FeMnP_{0.67}Sn_{0.33}$
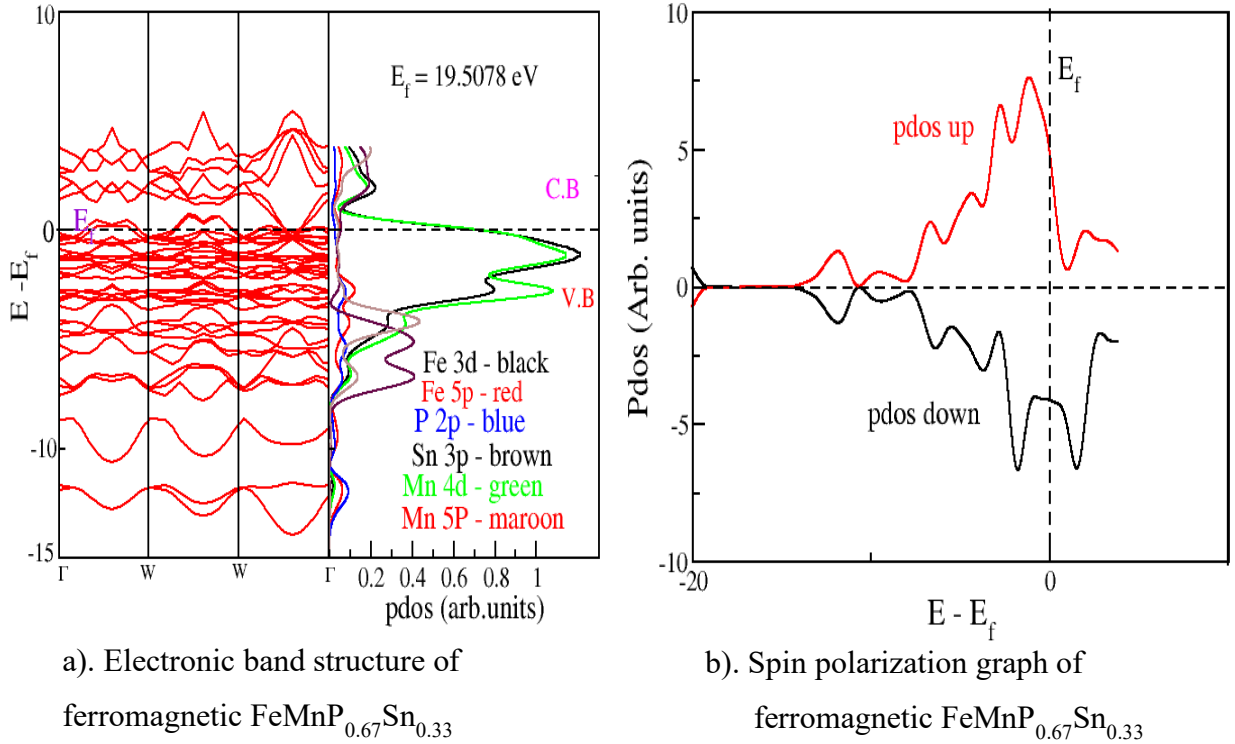
Figure 4. 5: Electronic band structure and spin polarisation graph for FM $FeMnP_{0.67}Sn_{0.33}$

Comparing figures 4.1b 4.3b 4.5b and 4.5b, that is FeMnP-(Si In, Se and Sn), spin-polarised graphs, it is clear that there are some similarities between 4.3b and 4.5b due to large atomic radii of Sn and In that is, the projection of the total PDOS above E_f is similar in both cases. The atomic radius of Sn is 1.88 Å while that of In is 1.95 Å (Glidewell, 1976; Nelson, 2018). In Figures 4.1b and 4.4b, the projection of total PDOS after E_f indicates some similarities due to almost the same atomic radii of Si and Se. Si has an atomic radius of 1.55 Å while Se has an atomic radius of 1.58 Å (Glidewell, 1976). This work was also investigated by Nelson (2018) whose results were consistent with Glidewell (1976).

In Figure 4.4b there is unsymmetrical nature of total PDOS below and above E_f than others hence large local magnetic moments (Hofer & Fisher, 2002). This result is confirmed by the calculated total magnetisation in Table 4.2. Excluding the base structure ($FeMnP_{0.67}Si_{0.33}$), in all other band structures of individual systems after the introduction of a dopant atom, it was observed that Mn and Fe play a key role in the magnetic nature of the system. It was realised that a flat band appearing just under the E_f was due to the majority of spin bands, which correspond to the Mn 4s orbital. This is derived from the local density of states (LDOS). In the case of minority spin, the

40

Mn atom introduces localised states with d-orbital character near the E_f in the CB, which can also be concluded from the minority d-orbital (Coleman *et al.,* 2011). The majority and minority spin channels could be noticed in the PDOS plot for individual orbitals at electronic band structure figures (Paudel *et al.,* 2016; She & Gupta, 2020).

4.5 Antiferromagnetic states of FeMnP-A (A=In, Se, Sn)

The two spin channels are symmetric for the AFM state of all of the compounds, indicating the disappearance of the overall magnetic moment of the AFM phase (Ma *et al.,* 2017). Comparing the electronic PDOS of the AFM and FM phases, significant electronic redistribution occurs during the phase transition (Lee *et al.,* 2017). To estimate the evolution of the bonding characteristics and local magnetic moment with the phase transition, PDOS were plotted which showed electron distribution. Electrons of 3d orbitals in the Fe and 4d orbitals of Mn atoms overlap as shown in Figure 4.5a. There is no electron cloud above E_f, in the spin-polarised graph for $FeMnP_{0.67} Si_{0.33}$. The graph showed no local magnetic moments as shown in figure 4.2b. Therefore, the substitution of Si was done to get some electron cloud above E_f.

For $FeMnP_{1-x}A_x$ (A= In. Se and Sn), the spin-up and spin-down channels of Fe become symmetric, indicating the disappearance of the local magnetic moment at the 3f Fe site (Ma *et al.,* 2017). These results indicated that the occupation of P atoms on different sites is significantly important for the magnetic properties of this family of compounds. The electronic distribution between Fe and Mn atoms with different magnetic polarisation is symmetric for AFM (figures 4.5, 4.6 and 4.7). This result was consistent with the findings of Zhang *et al.* (2019). There is more electron density between Fe and Mn atoms, it is found in Figure 4.5a that PDOS for Fe and Mn dominates consequently displaying more electron density. This observation on electron density between Fe and Mn indicates that the 3f-Fe site of $FeMnP_{1-x}A_x$ (A= In. Se and Sn) cannot show spin polarisation in the AFM states due to large overlap in the electron cloud between Fe and Mn occurs (Ma *et al.,* 2017). This, therefore, leads to kinetic energy which is lower for the spin degenerate states and leads to a decrease in the magnetic moment (Kang & Vafek, 2019).

4.5.1 Antiferromagnetic phase of $FeMnP_{0.67} In_{0.33}$

Figure 4.6a shows the band structure for AFM $FeMnP_{0.67} In_{0.33}$, the E_f lies on top of the VB. The electronic band structure was obtained along the high symmetry path $\Gamma - K - X - \Gamma$ as indicated in Figure 4.6a. CB overlaps VB showing that the material possesses metallic properties.

Figure 4.6b presents a spin-polarised graph of FeMnP$_{0.67}$In$_{0.33}$ with symmetrical nature between PDOS up and PDOS down. This shows the absence of local magnetic moments hence non-magnetic material. Total PDOS indicates the magnetic nature of FeMnP$_{0.67}$In$_{0.33}$ system and is calculated as $0.0\mu_B$ per cell as a total magnetic moment. It can be found that in the AFM configuration, the two spin contributions are the same, as its ground state is non-magnetic. The corresponding bonding states in the VB are all doubly occupied indicating that the total magnetisation is zero.

a) Electronic band structure of antiferromagnetic FeMnP$_{0.67}$In$_{0.33}$

b). Spin polarization graph of antiferromagnetic FeMnP$_{0.67}$In$_{0.33}$

Figure 4. 6: Electronic band structure and spin polarization graphs for AFM FeMnP$_{0.67}$In$_{0.33}$

4.5.2 Antiferromagnetic phase of FeMnP$_{0.67}$Se$_{0.33}$

Figure 4.7a is a presentation of the band structure for FeMnP$_{0.67}$Se$_{0.33}$, obtained along the high symmetry path $\Gamma - K - K - \Gamma$, the E$_f$ lies on VB. There is a high projection from Fe 3d and Mn 4d orbitals, a new feature is observed in PDOS where the high projection is witnessed from Se 2p orbital, Mn 4d orbitals and Fe 3d orbital. The emergence of high PDOS from Se which was not there during the FM phase may be a result of a missing bond in the AFM phase hence instability during magnetic phase transition (Cervantes *et al.,*2021).

Figure 4.7b shows the spin polarisation graph of $FeMnP_{0.67}Se_{0.33}$ with symmetrical nature between PDOS up and PDOS down. This is evidence of some non-magnetic nature of the material. Total PDOS indicates the magnetic nature of $FeMnP_{0.67}Se_{0.33}$ system and is calculated as $0.0 \mu_B$ per cell as a total magnetic moment. It is shown that in the AFM configuration, the two spin contributions are the same, as its ground state is non-magnetic. On the other hand, the corresponding bonding states in the VB are all doubly occupied signifying that the total magnetisation is zero.
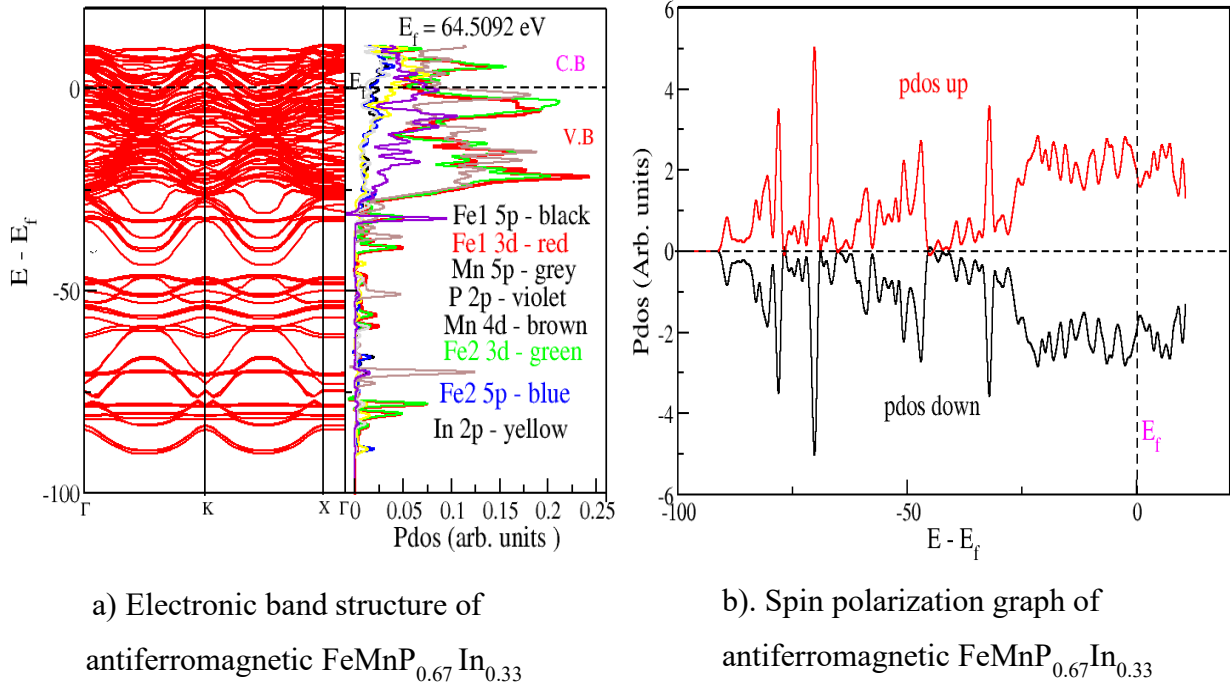

a) Electronic band structure of antiferromagnetic $FeMnP_{0.67}Se_{0.33}$

b). Spin polarization graph of antiferromagnetic $FeMnP_{0.67}Se_{0.33}$
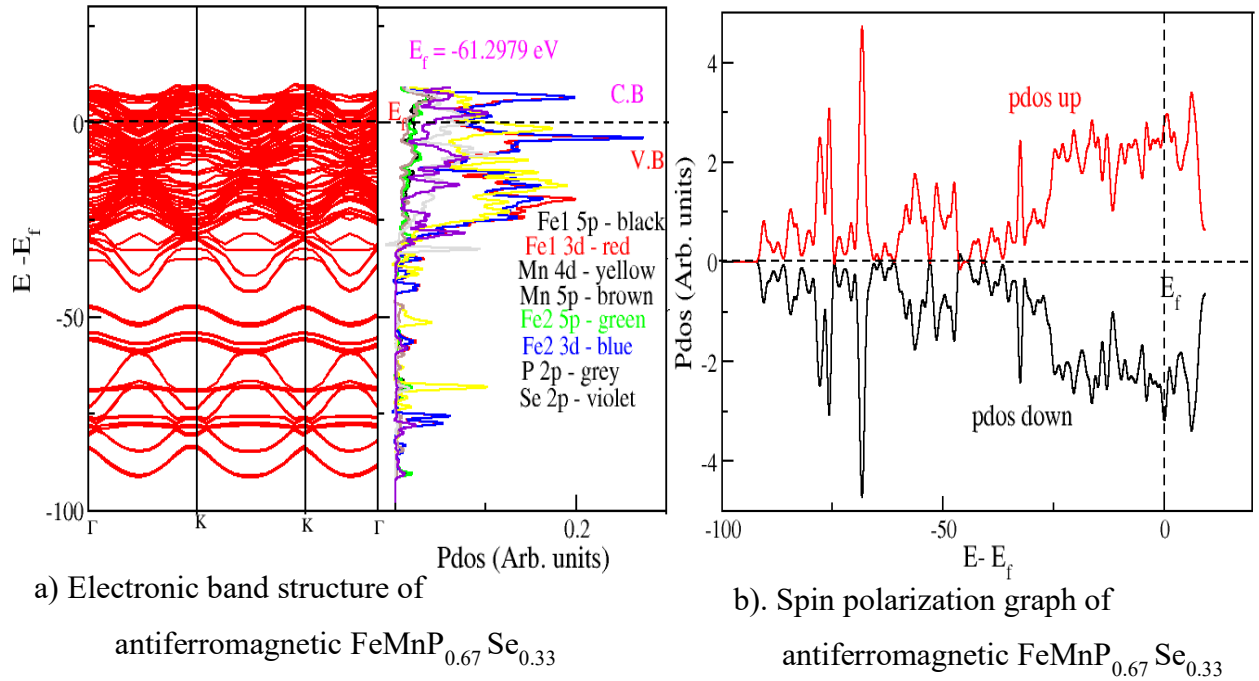
Figure 4. 7: Electronic band structure and spin polarization graph for AFM $FeMnP_{0.67}Se_{0.33}$

In Figure 4.8a, the band structure of $FeMnP_{0.67}Sn_{0.33}$, attained along the high symmetry path Γ – X – W – Γ, with E_f on top of VB as shown earlier in the FM phase thus metallic properties are preserved during phase transition. The PDOS states are mostly occupied by Sn 2p orbitals. In the FM phase, only Fe 3d orbital and Mn 4d orbitals were dominating in PDOS but in AFM, the case is different as Sn is now having more electron density than other atoms. This electron density exhibited only in the AFM phase may have contributed to bonding during the FM phase which is why it was not projected in the FM phase. This can be considered as an instability during the phase transition from FM to AFM phase as bonding in the system is not maintained (Rakel *et al.*, 2008).

In Figure 4.7b, the relationship between spin up and spin down is perfect symmetry indicating non-magnetic material.
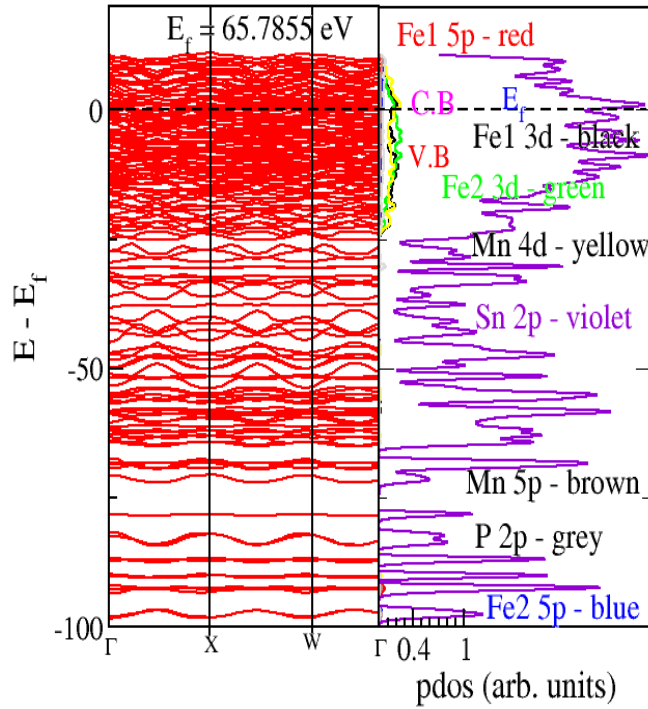
a) Electronic band structure of antiferromagnetic FeMnP$_{0.67}$Sn$_{0.33}$
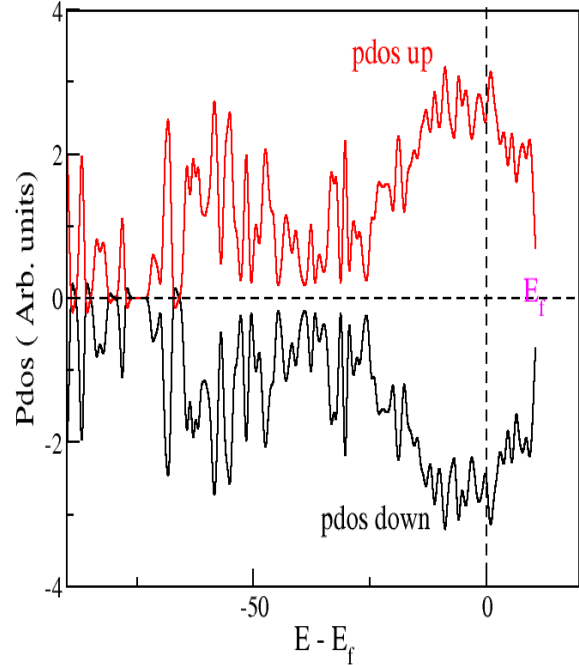
b). Spin polarization graph of antiferromagnetic FeMnP$_{0.67}$Sn$_{0.33}$

Figure 4. 8: Electronic band structure and spin polarization graphs for AFM FeMnP$_{0.67}$Sn$_{0.33}$

4.6 Magnetisation measurement

Total magnetisation refers to the difference between the number of spin-up and spin-down electrons in the cell of the system. The total absolute magnetisation is integral to the absolute polarisation density of the electrons per cell. Table 4.2 is a presentation of magnetisation in Bohr magneton per cell. From Table 4.2, AFM (18 atoms per cell) phases showed non-magnetic properties since the value of magnetisation per cell ranges from -0.2 to 0.22 (Bohr) mag/cell. All FM phases exhibited a range of values from 9.62 to 10.75 (Bohr) mag/cell. Given Table 4.2 it is very clear that In as a dopant is the best magnetic refrigerant as $FeMnP_{0.67}In_{0.33}$ showed the highest magnetisation of 10.75 (Bohr) mag/cell. Its electronic structure also exhibited stability during the magnetic phase transition.

Considering $FeMnP_{0.67}Si_{0.33}$ as the base material, it is clear that only the system doped with indium recorded an increase in the magnetic moment while selenium and tin-based compounds recorded a reduction in magnetic moment.

Table 4.2: Absolute magnetisation and total magnetisation in µB per cell of FM and AFM phases

Material	Magnetic Phase	Absolute magnetisation (Bohr) mag/cell (μ_B)	Total magnetisation (Bohr) mag/cell (μ_B)
$FeMnP_{0.67}Si_{0.33}$	Ferromagnetic	10.62	9.81
	Antiferromagnetic	0.01	0.00
$FeMnP_{0.67}In_{0.33}$	Ferromagnetic	10.75	9.98
	Antiferromagnetic	0.03	-0.01
$FeMnP_{0.67}Se_{0.33}$	Ferromagnetic	9.74	9.02
	Antiferromagnetic	0.22	-0.20
$FeMnP_{0.67}Sn_{0.33}$	Ferromagnetic	10.39	9.64
	Antiferromagnetic	0.04	-0.00

The magnitude of the total local magnetic moment per cell is reduced from 9.81 μ_B in the ferromagnetic phase to 0.00 µB in the antiferromagnetic phase in $FeMnP_{0.67}Si_{0.33}$. By contrast, the

iron show weak local magnetism. Here the Fe moment vanishes in the AFM phase (0.00 μ_B). This implies that the electron density around the Fe sites changes drastically at the phase transition (Dung *et al.,* 2011).

4.7 Charge transfer

The base compound was considered to be $FeMnP_{0.67}Si_{0.33}$, after calculation of PDOS, the total charge per atom is presented in Table 4.3. Charge transfer per atom was then calculated after the introduction of new atoms in the alloy.

Table 4.3: Charge transfer

Compound	Atoms	Total charge density		Charge Transfer	
		FM	AFM	FM	AFM
$FeMnP_{0.67}Si_{0.33}$	Fe	16.3841	16.2440	-	-
	Mn	15.3671	15.3781	-	-
	P	3.9966	3.5333	-	-
	Si	3.0915	2.6661	-	-
$FeMnP_{0.67}In_{0.33}$	Fe	7.9239	4.8012	8.4602	11.4428
	Mn	7.9614	4.4187	7.4057	10.9594
	P	0.0967	0.1242	3.8999	3.4091
	In	0.1484	0.5741	-	-
$FeMnP_{0.67}Se_{0.33}$	Fe	7.9457	4.9034	8.4384	11.3406
	Mn	7.9739	4.6304	7.3932	10.7477
	P	0.0842	0.1317	3.9124	3.4016
	Se	0.0708	0.2498	-	-
$FeMnP_{0.67}Sn_{0.33}$	Fe	7.9507	2.9006	8.4334	13.3434
	Mn	7.9724	3.1790	7.3947	12.1991
	P	0.0974	0.1850	3.8992	3.3483
	Sn	10.0936	0.3801	-	-

As mentioned before, spin-polarised calculations on the isolated compound ($FeMnP_{0.67}Si_{0.33}$) and the doped systems were also performed. The obtained results of the magnetic moment for the isolated compound is 9.81 μB, whereas, in the doped system, it is 9.98 μB for the case of indium, 9.02 μB for the case of Se and 9.64 μB for the case of Sn.

The magnetisation difference between the base compound and In-doped systems is about 0.17 μB indicating that the interaction with the indium atom generates 0.17 paired electrons in this doped system with the estimated charge transfer (charge density transfer) of 8.4602 electrons in the Fe atom and 7.4057 electrons in Mn atoms. The magnetisation difference between the base compound and Se-doped systems is -0.79 μB indicating that the interaction with the Se atom reduces 0.79 paired electrons in this doped system with the estimated charge transfer of 8.384 electrons in the Fe atom and 7.3932 electrons in Mn atoms. The magnetisation difference between the isolated system and Sn-doped structure is -0.17 μB indicating that the interaction with the Sn atom reduces 0.17 paired electrons in this doped system with the estimated charge transfer of 8.4334 electrons in the Fe atom and 7.3947 electrons in Mn atoms.

Only indium doped system-generated extra electrons in the system that led to an increase in the magnetic moment of the doped system while both Se and Sn led to a reduction of paired electrons in the system hence reduced magnetic moments.

Variations of the crystal magnetisation within the doped system spin state occupations were analysed. The PDOS for the spin-up and spin-down states within the doped system was also calculated, focusing on the projection into the 2pz direction of orbitals in Fe and Mn atoms. Spin polarisation was done only on Fe and Mn since they are magnetic and most sensitive to the magnetic properties of the material.

4.8 Thermodynamic properties

Magnetic refrigeration materials normally work under constant pressure and raised temperature. Therefore, Gibbs free energy of compounds with distinct magnetic order was computed and compared with raising the temperature to determine curie temperature T$_c$ (Cam *et al.*, 2007). The Gibbs free energy is given as:

$$G(P,T;m) = \min \left[U(V;m) + F_{vib}(V,T;m) + F_{el}(V,T;m) + P(V,T;m)V \right] \qquad 6.2$$

Where m represents the FM or AFM magnetic state. The vibrational free energy was estimated by the Debye model (Otero *et al.*, 2011) and the free energy of thermal electronic excitation was calculated within the single electron excitation picture (Ma *et al.*, 2017).

The magnetic entropy of the AFM phase was approximated using the mean-field approximation (Grimvall, 1989): $S_m = K_B \sum_i \ln (\mu_i + 1)$, where μ_i is the magnetic moment at the ith site. The total Gibbs free energy of the AFM phase becomes:

$$G_{tot}(P,T) = G(P,T,AFM) - S_m T \qquad\qquad 6.3$$

The predicted T_C for FeMnP$_{0.67}$Si$_{0.33}$ is 460K, which is close to the findings by Delczeg *et al.* (2010) who found out that the AFM/FM transition temperature is found to increase with the increasing substitution, for example, T$_c$=216K for $x = 0$ and T$_c$=660 for $x = 0.35$ (Delczeg *et al.*, 2010). This verifies that the Thermo_pw programme interfaced with Quantum Espresso code gives a reliable prediction of the Curie temperature T$_c$. The difference between experiment and computational findings is attributed to the absence of entropy contributions from spin wave excitation and phonon-phonon interactions.

The Gibbs free energy difference $\Delta G(P,T) = G(P,T,AFM) - G(P,T,FM - S_m T)$ was computed for all compounds and presented in Fig. 10 (a) for comparison. $\Delta G(P,T)$ gradually diminishes and intersects with the x-axis at the curie temperature T$_c$ as shown in Figure 4.9 (a). The decrease of

$\Delta G(P,T)$ at raised temperature is predominantly from magnetic entropy. The unsteady slope of $\Delta G(P,T)$ indicates that the anharmonic effect plays a significant role.

a). Gibbs free energy change with temperature from AFM to FM

b). Entropy changes at the curie temperature T$_c$
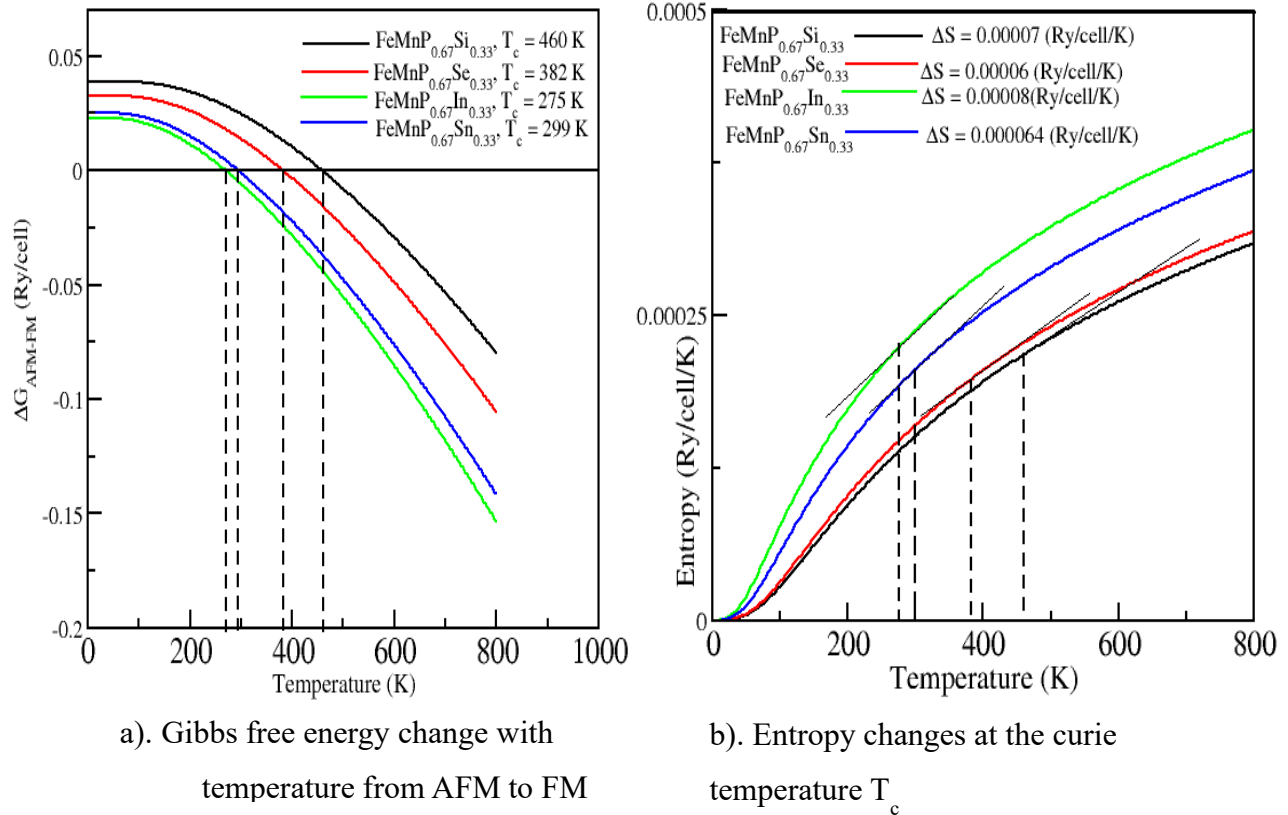
Figure 4. 9: Gibbs free energy change with temperature from AFM to FM and entropy change at curie temperature

The temperature dependence of the total entropy of the compounds is presented in Figure 4.9b. From Figure 4.9, the curie temperature of $FeMnP_{0.67}In_{0.33}$ is 275 K, whereas the magnetic entropy change at this curie temperature is 0.00008 (Ry/cell/K). These results are similar to Hu et al's findings (Hu *et al.,* 2002). Hu et al found that a large magnetic entropy change ΔS in a Fe-based compound near a curie temperature of 274 K, making the compound have great potential for applications as magnetic refrigerants near room temperature. These results show that $FeMnP_{0.67}In_{0.33}$ has the largest magnetic entropy change ΔS, therefore it is expected that this compound could be a candidate for near-room temperature magnetic refrigeration.

CHAPTER FIVE

CONCLUSIONS AND RECOMMENDATIONS

5.1 Conclusions

In this work, a computational study of magnetic properties of $FeMnP_{1-x}A_x$ (A = In, Se and Sn, where x = 0.33) is reported using density functional theory (DFT) which is the first principle calculation within the Quantum ESPRESSO method, thermos-pw interfaced within QE, with GGA exchange-correlation functional. These calculations were able to investigate magnetic characteristics in both FM and AFM phases of hexagonal $FeMnP_{1-x}A_x$ (A = In, Se and Sn, where x = 0.33) as a candidate for magnetic refrigerant. Since Fe and Mn belong to transition metals with partially filled d-subshell, for electronic structure calculations, spin polarisation had to be considered. Also, the *ab-initio* calculations were used to examine the effects of magnetic transition on the ground state properties of this compound. The calculations in this study were based on the DFT which is strictly valid for the ground state. The hexagonal $FeMnP_{1-x}A_x$ (A = In, Se and Sn, where x = 0.33) structure was found to have a metallic nature in both FM and AFM phases.

It has been found from the outcomes that when the stable FeMnP phase is doped with silicon, compound $FeMnP_{0.67}Si_{0.33}$ is unstable along the magnetic phase transition since there was a change in the metallic structure. This was exhibited by a change in the compound electronic band structure of the AFM phase of the material. There were DOS in the empty band states of the AFM phase but in the FM phase, all the bands were occupied by DOS showing some instability. This instability feature necessitated the replacement of zinc with other viable elements.

The calculated values of magnetisation showed that when the unstable Si element was replaced with atoms of post-transitional metals that are In and Sn, it was found that In was probably the best replacement for Si among the studied elements. Se as non-metal was also included in the list of dopants but still In showed the best results. Also, from this study, it can be found that the nature of the system in both FM ordering and AFM ordering is metallic. This is evidenced by, the DOS starting from the bottom of the valance band and filling up to the E_f. Since the CB and VB are overlapping, the E_f is in CB and there are plenty of electrons available for conducting. From Table 4.2, when In was introduced into the alloy, it produced the highest value of total magnetisation per cell in the FM phase. When the Si atom was replaced by In, it generated extra paired electrons in the system unlike atoms of Se and Sn which showed a reduction in paired electrons thus reducing the magnetic moments of the doped system. In the case of FM order, when

the spins are oriented parallel to each other, the magnetic energy is minimised. For that reason, the material may turn into a strong magnet in the presence of an externally applied magnetic field. Also, in the case of AFM order, the magnetic energy is minimised when pairs of nearby spins are oriented antiparallel to each other. This state proposes that the signs of the magnetic interactions in an AFM are opposite those in a ferromagnet.

Magnetic-elastic susceptibility is referred to as a theoretical quantity that describes the deformation or strain of a material under the influence of an applied magnetic field and how the material changes its structure along the magnetic phase transition. All the dopants showed stability in the system along the magnetic phase transition, unlike the Si which showed some deformation as the material was transiting from the FM to AFM phase. In was most preferred due to its good magnetic properties.

5.2 Recommendations

i. This work only dealt with magnetic properties of $FeMnP_{1-x}A_x$ (A = Si, In, Se and Sn) alloys. There is a need to study the electronics, mechanical and structural properties of the same alloys since their magnetic properties were very close to experimental findings.

ii. Phonon of $FeMnP_{1-x}A_x$ (A = Si, In, Se and Sn) alloys should also be investigated to determine the thermal conductivity of these alloys.

iii. The study worked with ratio $FeMnP_{1-x}A_x$ (A = Si, In, Se and Sn), where x = 0.33, there is also a need to vary the ratio and interchange the value of x to confirm the results both experimentally and theoretically.

iv. The study used a theoretical approach to study the magnetic properties of $FeMnP_{1-x}A_x$ (A = Si, In, Se and Sn) alloys, Consequently, there is a need to carry out an experimental investigation on the same alloys in the same ratio.

REFERENCES

Anisimov, V. I., Zaanen, J., & Andersen, O. K. (1991). Band theory and Mott insulators: Hubbard*U*instead of Stoner I. *Physical Review B*, *44*(3), 943-954. https://doi.org/10.1103/physrevb.44.943

Balli, M., Sari, O., Zamni, L., Mahmed, C., & Forchelet, J. (2012). Implementation of La(Fe, Co)13−xSix materials in magnetic refrigerators: Practical aspects. Materials Science and Engineering: B, 177(8), 629-634. https://doi.org/10.1016/j.mseb.2012.03.016

Bazine, W., Tahiri, N., El Bounagui, O., Ez-Zahraouy, H., & Benyoussef, A. (2019). Structural, electronic, magnetic, and magnetocaloric properties in intermetallic compound TbCu2Si2. *Journal of Magnetism and Magnetic Materials*, *481*, 72-76. https://doi.org/10.1016/j.jmmm.2019.02.095

Behrsing, T., Deacon, G., & Junk, P. (2014). The chemistry of rare earth metals, compounds, and corrosion inhibitors. *Rare Earth-Based Corrosion Inhibitors*, 1-37. https://doi.org/10.1533/9780857093585.1

Blanc, X., Cancès, E., & Dupuy, M. (2019). Variational projector augmented-wave method: Theoretical analysis and preliminary numerical results. *Numerische Mathematik*, *144*(2), 271-321. https://doi.org/10.1007/s00211-019-01082-2

Blöchl, P. E. (1994). Projector augmented-wave method. *Physical Review B*, *50*(24), 17953-17979. https://doi.org/10.1103/physrevb.50.17953

Blöchl, P. E., Jepsen, O., & Andersen, O. K. (1994). Improved tetrahedron method for brillouin-zone integrations. *Physical Review B*, *49*(23), 16223-16233. https://doi.org/10.1103/physrevb.49.16223

Bohigas, X., Molins, E., Roig, A., Tejada, J., & Zhang, X. (2000). Room-temperature magnetic refrigerator using permanent magnets. *IEEE Transactions on Magnetics*, *36*(3), 538-544. https://doi.org/10.1109/20.846216

Bohigas, X., Tejada, J., Torres, F., Arnaudas, J. I., Joven, E., & Del Moral, A. (2002). Magnetocaloric effect in random magnetic anisotropy materials. *Applied Physics Letters*, *81*(13), 2427-2429. https://doi.org/10.1063/1.1506777

Brück, E., Tegus, O., Li, X., De Boer, F., & Buschow, K. (2003). Magnetic refrigeration—towards room-temperature applications. *Physica B: Condensed Matter*, *327*(2-4), 431-437. https://doi.org/10.1016/s0921-4526(02)01769-6

Brück, E., Tegus, O., Thanh, D., & Buschow, K. (2007). Magnetocaloric refrigeration near room temperature (invited). *Journal of Magnetism and Magnetic Materials*, *310*(2), 2793-2799. https://doi.org/10.1016/j.jmmm.2006.10.1146

Burke, K., Perdew, J. P., & Levy, M. (1995). Semilocal density functionals for exchange and correlation: Theory and applications. *Theoretical and Computational Chemistry*, 29-74. https://doi.org/10.1016/s1380-7323(05)80032-9

Burke, K., Perdew, J. P., & Wang, Y. (1998). Derivation of a generalized gradient approximation: The PW91 density functional. *Electronic Density Functional Theory*, 81-111. https://doi.org/10.1007/978-1-4899-0316-7_7

Cam Thanh, D., Brück, E., Tegus, O., Klaasse, J., & Buschow, K. (2007). Influence of SI and GE on the magnetic phase transition and magnetocaloric properties of MnFe(P,Si,Ge). *Journal of Magnetism and Magnetic Materials*, *310*(2), e1012-e1014. https://doi.org/10.1016/j.jmmm.2006.11.194

Cenni, R. (1991). Functional techniques in the many-body problem the longitudinal nuclear response function. *Condensed Matter Theories*, 429-441. https://doi.org/10.1007/978-1-4615-3686-4_35

Cervantes, J. M., Pilo, J., Rosas-Huerta, J. L., Antonio, J. E., Muñoz, H., Oviedo-Roa, R., & Carvajal, E. (2021). DFT electronic properties and synthesis thermodynamics of Li_X $La1−x$ TiO3 electrolytes for Li-ion batteries. *Journal of The Electrochemical Society*, *168*(8), 080516. https://doi.org/10.1149/1945-7111/ac1a52

Charif Alaoui, Y., Tahiri, N., El Bounagui, O., & Ez-Zahraouy, H. (2020). Magnetocaloric effect in metallic antiperovskite Mn3InC compound: AB-initio study and Monte Carlo simulations. *Solid State Communications*, *309*, 113841. https://doi.org/10.1016/j.ssc.2020.113841

Cicek, M., Saritas, S., Yildirim, O., & Emre, B. (2020). Effect of the low constituent boron on martensitic transformation, magnetic, and magnetocaloric properties of Ni50Mn35In15 Heusler alloys. *Journal of Alloys and Compounds*, *845*, 155493. https://doi.org/10.1016/j.jallcom.2020.155493

Coleman, J. N., Lotya, M., O'Neill, A., Bergin, S. D., King, P. J., Khan, U., Young, K., Gaucher, A., De, S., Smith, R. J., Shvets, I. V., Arora, S. K., Stanton, G., Kim, H., Lee, K., Kim, G. T., Duesberg, G. S., Hallam, T., Boland, J. J., Wang, J.J., John, F.D., Jaime, C.G.,

Gregory, M., Aleksey, S., Rebecca, J.N. & Nicolosi, V. (2011). Two-dimensional Nanosheets produced by liquid exfoliation of layered materials. *Science*, *331*(6017), 568-571. https://doi.org/10.1126/science.1194975

Dan'kov, S. Y., Ivtchenko, V. V., Tishin, A. M., Gschneidner, K. A., & Pecharsky, V. K. (2000). Magnetocaloric effect in GdAl2 and Nd2Fe17. *Advances in Cryogenic Engineering Materials*, 397-404. https://doi.org/10.1007/978-1-4615-4293-3_51

Debye, P. (1926). Einige Bemerkungen zur Magnetisierung bei tiefer Temperatur. *Annalen der Physik*, *386*(25), 1154-1160. https://doi.org/10.1002/andp.19263862517

Delczeg-Czirjak, E. K., Delczeg, L., Punkkinen, M. P., Johansson, B., Eriksson, O., & Vitos, L. (2010). *Ab initio*study of structural and magnetic properties of Si-doped "http://www.w3.org/1998/Math/MathML" *Physical Review B*, *82*(8), 085103. https://doi.org/10.1103/physrevb.82.085103

Dennis, C. L., & Ivkov, R. (2013). Physics of heat generation using magnetic nanoparticles for hyperthermia. *International Journal of Hyperthermia*, *29*(8), 715-729. https://doi.org/10.3109/02656736.2013.836758

Dong, Z., Wang, Z., & Yin, S. (2020). Magnetic properties and magneto-caloric effect (MCE) in Cu22Al18Ho22Tm20Gd18 amorphous ribbons. *Journal of Magnetism and Magnetic Materials*, *514*, 167270. https://doi.org/10.1016/j.jmmm.2020.167270

Dreizler, R. M., & Gross, E. K. (1983). Density functional approach to the relativistic many body problem. *Quantum Electrodynamics of Strong Fields*, 383-412. https://doi.org/10.1007/978-1-4899-2139-0_16

Dubrovin, V., Popov, A., & Avdoshenko, S. (2020). Valence electrons in lanthanide-based single-atom magnets: A paradigm shift in 4f-Magnetism modeling and design. https://doi.org/10.26434/chemrxiv.12800096

Dung, N. H., Ou, Z. Q., Caron, L., Zhang, L., Thanh, D. T., De Wijs, G. A., De Groot, R. A., Buschow, K. H., & Brück, E. (2011). Mixed magnetism for refrigeration and energy conversion. *Advanced Energy Materials*, *1*(6), 1215-1219. https://doi.org/10.1002/aenm.201100252

Ekanth, V. P., & Kishor, F. (2016). New Eco-friendly Magnetic Refrigeration System. *International Research Journal of Engineering and Technology*, *3*, 1512-13. https://www.academia.edu/34652299/New_Eco_friendly_Magnetic_Refrigeration_System

Fleig, T. (2012). Invited review: Relativistic wave-function based electron correlation methods. *Chemical Physics*, *395*, 2-15. https://doi.org/10.1016/j.chemphys.2011.06.032

Foldeaki, M., Schnelle, W., Gmelin, E., Benard, P., Koszegi, B., Giguere, A., Chahine, R., & Bose, T. K. (1997). Comparison of magnetocaloric properties from magnetic and thermal measurements. *Journal of Applied Physics*, *82*(1), 309-316. https://doi.org/10.1063/1.365813

Franco, V., Blázquez, J., Ingale, B., & Conde, A. (2012). The Magnetocaloric effect and magnetic refrigeration near room temperature: Materials and models. *Annual Review of Materials Research*, *42*(1), 305-342. https://doi.org/10.1146/annurev-matsci-062910-100356

Franco, V., Blázquez, J., Ipus, J., Law, J., Moreno-Ramírez, L., & Conde, A. (2018). Magnetocaloric effect: From materials research to refrigeration devices. *Progress in Materials Science*, *93*, 112-232. https://doi.org/10.1016/j.pmatsci.2017.10.005

Giannozzi, P., Andreussi, O., Brumme, T., Bunau, O., Buongiorno Nardelli, M., Calandra, M., Car, R., Cavazzoni, C., Ceresoli, D., Cococcioni, M., Colonna, N., Carnimeo, I., Dal Corso, A., De Gironcoli, S., Delugas, P., DiStasio, R. A., Ferretti, A., Floris, A., Fratesi, G., Gorni T., Jia J., Kawamura M., Ko H-Y., Kokalj A., Küçükbenli E., Lazzeri M., Marsili M., Marzari N., Mauri F., Nguyen N. L, Nguyen H., Otero-de-la-Roza A., Paulatto A., Poncé S., Rocca D., Sabatini R., Santra B., Schlipf M., Seitsonen P., Smogunov P, Timrov I, Thonhauser T., Umari P., Vast N., Wu X & Baroni, S. (2017). Advanced capabilities for materials modelling with quantum espresso. *Journal of Physics: Condensed Matter*, *29*(46), 465901. https://doi.org/10.1088/1361-648x/aa8f79

Giannozzi, P., Baroni, S., Bonini, N., Calandra, M., Car, R., Cavazzoni, C., Ceresoli, D., Chiarotti, G. L., Cococcioni, M., Dabo, I., Dal Corso, A., De Gironcoli, S., Fabris, S., Fratesi, G., Gebauer, R., Gerstmann, U., Gougoussis, C., Kokalj, A., Lazzeri, M., Martin. M., Marzari, N., Francesco, M., Ricaardo, M., Stefano, P., Alfredo, P., Lorenzo, P., Sando S. & Wentzcovitch, R. M. (2009). Quantum espresso: A modular and open-source software project for quantum simulations of materials. *Journal of Physics: Condensed Matter*, *21*(39), 395502. https://doi.org/10.1088/0953-8984/21/39/395502

Giauque, W. F. (1927). A thermodynamic treatment of certain magnetic effects. A proposed method of producing temperatures considerably below 1° absolute. *Journal of the American Chemical Society*, *49*(8), 1864-1870. https://doi.org/10.1021/ja01407a003

Glidewell, C. (1976). Intramolecular non-bonded atomic radii: Application to the heavier P elements. *Inorganica Chimica Acta*, *20*, 113-118. https://doi.org/10.1016/s0020-1693(00)94101-x

Gombi, S. M., & Sahu, D. (2020). A review on magneto-caloric materials for room temperature refrigeration. *International Journal of Automotive and Mechanical Engineering*, *17*(1), 7805-7815. https://doi.org/10.15282/ijame.17.1.2020.26.0581.

Gomès, S., Assy, A., & Chapuis, P. (2015). Scanning thermal microscopy: A review. *Physica Status Solidi (a)*, *212*(3), 477-494. https://doi.org/10.1002/pssa.201400360

Grimvall, G. (1989). Spin disorder in paramagnetic FCC iron. *Physical Review B*, *39*(16), 12300-12301. https://doi.org/10.1103/physrevb.39.12300

Gschneidner, K. A., & Pecharsky, V. K. (1999). Magnetic refrigeration materials (invited). *Journal of Applied Physics*, *85*(8), 5365-5368. https://doi.org/10.1063/1.369979

Gschneidner, K. A., & Pecharsky, V. K. (2000). Magnetocaloric materials. *Annual Review of Materials Science*, *30*(1), 387-429. https://doi.org/10.1146/annurev.matsci.30.1.387

Hamad, M. A. (2015). Calculations of the low-field Magnetocaloric effect in Fe4MnSi3B X. *Journal of Superconductivity and Novel Magnetism*, *28*(7), 2223-2227. https://doi.org/10.1007/s10948-015-3025-6

Hao, X., Ohtsuka, H., & Wada, H. (2005). Variation of phase transformation temperature in fe-C alloys in a high magnetic field. *Materials Processing in Magnetic Fields*. https://doi.org/10.1142/9789812701800_0005

Harutyunyan, S. R. (2004). Thermopower, transport properties of (LaxCe1−x)B6 Kondo systems and thermoelectric refrigeration utilizing CeB6 single crystal at cryogenic temperatures. *AIP Conference Proceedings*. https://doi.org/10.1063/1.1774741

Hessell, E. T. (2013). Next generation refrigeration lubricants for low global warming potential/Low ozone depleting refrigeration and air conditioning systems. https://doi.org/10.2172/1113040

Hofer, W., & Fisher, A. (2002). Determining surface magnetization and local magnetic moments with atomic scale resolution. *Surface Science*, *515*(2-3), L487-L492. https://doi.org/10.1016/s0039-6028(02)02025-3

Hohenberg, P., & Kohn, W. (1964). Inhomogeneous electron gas. *Physical Review*, *136*(3B), B864-B871. https://doi.org/10.1103/physrev.136.b864

Hu, F. X., Qian, X. L., Sun, J. R., Wang, G. J., Zhang, X. X., Cheng, Z. H., & Shen, B. G. (2002). Magnetic entropy change and its temperature variation in compounds La(Fe1−xCox)11.2Si1.8. *Journal of Applied Physics*, *92*(7), 3620-3623. https://doi.org/10.1063/1.1502919

Hu, F., Shen, B., Sun, J., Wang, G., & Cheng, Z. (2002). Very large magnetic entropy change near room temperature in LaFe11.2Co0.7Si1.1. *Applied Physics Letters*, *80*(5), 826-828. https://doi.org/10.1063/1.1447592

Hu, J., Guan, L., Fu, S., Sun, Y., & Long, Y. (2014). Corrosion and latent heat in thermal cycles for La(Fe,Mn,Si)13 magnetocaloric compounds. *Journal of Magnetism and Magnetic Materials*, *354*, 336-339. https://doi.org/10.1016/j.jmmm.2013.11.025

Huang, C. (2018). Embedded cluster density approximation for exchange–correlation energy: A natural extension of the local density approximation. *Journal of Chemical Theory and Computation*, *14*(12), 6211-6225. https://doi.org/10.1021/acs.jctc.8b00471

Kaneyoshi, T. (2020). On the possibility of magnetic ordering (TC(N)) induced by a surface exchange interaction in an Ising nanoparticle with TC(N) > TC(B), where TC(B) is a transition temperature in the corresponding bulk system. *Chemical Physics*, *530*, 110588. https://doi.org/10.1016/j.chemphys.2019.110588

Kang, J., & Vafek, O. (2019). Strong coupling phases of partially filled twisted Bilayer Graphene narrow bands. *Physical Review Letters*, *122*(24). https://doi.org/10.1103/physrevlett.122.246401

Kang, J., & Vafek, O. (2019). Strong coupling phases of partially filled twisted Bilayer Graphene narrow bands. *Physical Review Letters*, *122*(24). https://doi.org/10.1103/physrevlett.122.246401

Kohn, W., & Mattsson, A. E. (1998). Edge electron gas. *Physical Review Letters*, *81*(16), 3487-3490. https://doi.org/10.1103/physrevlett.81.3487

Kotelnikova, O., Prudnikov, V., & Rudoy, Y. (2015). Magnetocaloric effect (MCE): Microscopic approach within Tyablikov approximation for anisotropic ferromagnets. *Journal of Magnetism and Magnetic Materials*, *383*, 203-207. https://doi.org/10.1016/j.jmmm.2014.11.030

Kulińska, A., Wodniecka, B., & Wodniecki, P. (2006). The perturbed angular correlation studies of ag–zr compounds with 111Cd probes. *Journal of Alloys and Compounds*, *426*(1-2), 76-82. https://doi.org/10.1016/j.jallcom.2006.04.028

Lee, J. H., Choi, W. S., Jeen, H., Lee, H., Seo, J. H., Nam, J., Yeom, M. S., & Lee, H. N. (2017). Strongly coupled magnetic and electronic transitions in multivalent strontium cobaltites. *Scientific Reports*, *7*(1). https://doi.org/10.1038/s41598-017-16246-z

Li, Y., Lin, G., & Chen, J. (2021). Numerical investigation and performance evaluation of the mnfe-based composite magnetocaloric material with large magnetic entropy change over a wide temperature range. *International Journal of Refrigeration*, *121*, 61-71. https://doi.org/10.1016/j.ijrefrig.2020.10.004

Liang, W., & Whangbo, M. (1993). Conductivity anisotropy and structural phase transition in covellite CuS. *Solid State Communications*, *85*(5), 405-408. https://doi.org/10.1016/0038-1098(93)90689-k

Liu, Y., Jing, C., He, X., Zhang, Y., Xu, K., & Li, Z. (2017). Inverse magnetocaloric effect and magnetoresistance associated with martensitic transition for CU-doped Ni-mn-In Heusler alloy. *Physica Status Solidi (a)*, *214*(6), 1600906. https://doi.org/10.1002/pssa.201600906

Ma, S., Wurentuya, B., Wu, X., Jiang, Y., Tegus, O., Guan, P., & Narsu, B. (2017). AB initio mechanical and thermal properties of FeMnP1−xGax compounds as refrigerant for room-temperature magnetic refrigeration. *RSC Advances*, *7*(44), 27454-27463. https://doi.org/10.1039/c7ra04274d

Madireddi, S. C. (2010). *Role of extrinsic factors in utilizing the Giant Magnetocaloric Effect on materials: Frequency and time dependence*. Iowa State University. https://doi.org/10.31274/etd-180810-141

Makov, G., & Payne, M. C. (1995). Periodic boundary conditions in *ab initio* calculations. *Physical Review B*, *51*(7), 4014-4022. https://doi.org/10.1103/physrevb.51.4014

Mao, P., Yu, B., Liu, Z., Wang, F., & Ju, Y. (2013). First-principles calculations of structural, elastic and electronic properties of AB2 type intermetallics in mg–zn–Ca–Cu alloy. *Journal of Magnesium and Alloys*, *1*(3), 256-262. https://doi.org/10.1016/j.jma.2013.10.001

McLinden, M. O., Brown, J. S., Brignoli, R., Kazakov, A. F., & Domanski, P. A. (2017). Limited options for low-global-warming-potential refrigerants. *Nature Communications*, *8*(1), 14476. https://doi.org/10.1038/ncomms14476

Miao, X., Caron, L., Gubbens, P., Yaouanc, A., Dalmas de Réotier, P., Luetkens, H., Amato, A., Van Dijk, N., & Brück, E. (2016). Spin correlations in (Mn,Fe)2(P,Si) magnetocaloric

compounds above Curie temperature. *Journal of Science: Advanced Materials and Devices*, *1*(2), 147-151. https://doi.org/10.1016/j.jsamd.2016.06.002

Modak, J. K., Ariful, P., & Nahid, I. (2015). Spin-Polarization-and-Electronic-Structure-calculation-of-Nickel-and-Co$_2$MnSi-thin-film-interface. *doc Int. J. Sci. Eng. Res*, 6(8), 538-545. https://doi.org/10.1063/5.0076246

Monkhorst, H. J., & Pack, J. D. (1976). Special points for brillouin-zone integrations. *Physical Review B*, *13*(12), 5188-5192. https://doi.org/10.1103/physrevb.13.5188

Mulwa, W. M. (2012). *Structural and electronic studies of Tio 2, Cr: Tio 2 And Nb: Tio 2 using Density Functional Theory* (M.Sc. dissertation, Moi University).

Nelson, D. (2018). Atomic radius trend. *Science Trends*. https://doi.org/10.31988/scitrends.17291

Otero-de-la-Roza, A., Abbasi-Pérez, D., & Luaña, V. (2011). Gibbs2: A new version of the quasiharmonic model code. II. Models for solid-state thermodynamics, features and implementation. *Computer Physics Communications*, *182*(10), 2232-2248. https://doi.org/10.1016/j.cpc.2011.05.009

Ou, Z. (2013). *Magnetic structure and phase formation of magnetocaloric Mn-Fe-P-X compounds*. Retrieved from http://repository.tudelft.nl/assets/uuid:4ba9f9cb-49fe-48a2-ab89-eb80070b7362/PhD_Thesis_-_ZHIQIANG.OU.pdf

Pal A., (2018). *Environmental assessment and characteristics of next generation refrigerants* (Doctoral dissertation, Kyushu University).

Paudel, B. P., Pantha, N., & Adhikari, N. P. (2015). First-principles study of electronic and magnetic properties of manganese decorated graphene. *Journal of Nepal Physical Society*, *3*(1), 24-34. https://doi.org/10.3126/jnphyssoc.v3i1.14439

Payne, M. C., Teter, M. P., Allan, D. C., Arias, T. A., & Joannopoulos, J. D. (1992). Iterative minimization techniques for *ab initio* total-energy calculations: Molecular dynamics and conjugate gradients. *Reviews of Modern Physics*, *64*(4), 1045-1097. https://doi.org/10.1103/revmodphys.64.1045

Pecharsky, V. K., & Gschneidner Jr, K. A. (1999). Magnetocaloric effect and magnetic refrigeration. *Journal of Magnetism and Magnetic Materials*, *200*(1-3), 44-56. https://doi.org/10.1016/s0304-8853(99)00397-2

Pecharsky, V. K., & Gschneidner Jr., K. A. (2001). Gd5(sixge1-x)4: An extremum material. *Advanced Materials*, *13*(9), 683-686. https://doi.org/10.1002/1521-4095(200105)13:9<683::aid-adma683>3.0.co;2-o

Pecharsky, V. K., & Gschneidner, K. A. (1996). Comparison of the Magnetocaloric effect derived from heat capacity, direct, and magnetization measurements. *Advances in Cryogenic Engineering Materials*, (pp. 423-430). https://doi.org/10.1007/978-1-4757-9059-7_56

Pecharsky, V. K., & Gschneidner, K. A. (1998). The giant Magnetocaloric effect in gd5(sixge1-x)4 materials for magnetic refrigeration. *Advances in Cryogenic Engineering*, 1729-1736. https://doi.org/10.1007/978-1-4757-9047-4_218

Pecharsky, V., & Gschneidner, K. (1997). Effect of alloying on the giant magnetocaloric effect of Gd5(Si2Ge2). *Journal of Magnetism and Magnetic Materials*, *167*(3), L179-L184. https://doi.org/10.1016/s0304-8853(96)00759-7

Pecharsky, V., Gschneidner, K., Pecharsky, A., & Tishin, A. (2001). Thermodynamics of the magnetocaloric effect. *Physical Review B*, *64*(14), 144406. https://doi.org/10.1103/physrevb.64.144406

Pecharsky, V., Samolyuk, G., Antropov, V., Pecharsky, A., & Gschneidner, K. (2003). The effect of varying the crystal structure on the magnetism, electronic structure and thermodynamics in the Gd 5 (SI X GE 1−x) 4 system near X =0.5. *Journal of Solid State Chemistry*, *171*(1-2), 57-68. https://doi.org/10.1016/s0022-4596(02)00146-9

Perdew, J. P., Chevary, J. A., Vosko, S. H., Jackson, K. A., Pederson, M. R., Singh, D. J., & Fiolhais, C. (1992). Atoms, molecules, solids, and surfaces: Applications of the generalized gradient approximation for exchange and correlation. *Physical Review B*, *46*(11), 6671-6687. https://doi.org/10.1103/physrevb.46.6671

Perdew, J. P., Chevary, J. A., Vosko, S. H., Jackson, K. A., Pederson, M. R., Singh, D. J., & Fiolhais, C. (1993). Erratum: Atoms, molecules, solids, and surfaces: Applications of the generalized gradient approximation for exchange and correlation. *Physical Review B*, *48*(7), 4978-4978. https://doi.org/10.1103/physrevb.48.4978.2

Perdew, J. P., Ruzsinszky, A., Csonka, G. I., Vydrov, O. A., Scuseria, G. E., Constantin, L. A., Zhou, X., & Burke, K. (2009). Erratum: Restoring the density-gradient expansion for exchange in solids and surfaces [Phys. Rev. Lett.100, 136406 (2008)]. *Physical Review Letters*, *102*(3). https://doi.org/10.1103/physrevlett.102.039902

Polvani, L. M., Previdi, M., England, M. R., Chiodo, G., & Smith, K. L. (2020). Substantial twentieth-century Arctic warming caused by ozone-depleting substances. *Nature Climate Change*, *10*(2), 130-133. https://doi.org/10.1038/s41558-019-0677-4

Rakel, M., Cobet, C., Esser, N., Fuchs, F., Bechstedt, F., Goldhahn, R., Schmidt, W. G., & Schaff, W. (2008). Gan and inn conduction-band states studied by ellipsometry. *Physical Review B*, *77*(11). https://doi.org/10.1103/physrevb.77.115120

Romero Gómez, J., Ferreiro Garcia, R., De Miguel Catoira, A., & Romero Gómez, M. (2013). Magnetocaloric effect: A review of the thermodynamic cycles in magnetic refrigeration. *Renewable and Sustainable Energy Reviews*, *17*, 74-82. https://doi.org/10.1016/j.rser.2012.09.027

Roy, P., Torun, E., & De Groot, R. A. (2016). Effect of doping and elastic properties in (Mn, Fe) 2 (Si, P). *Physical Review B*, *93*(9). https://doi.org/10.1103/physrevb.93.094110

Samanta, T., Lepkowski, D. L., Saleheen, A. U., Shankar, A., Prestigiacomo, J., Dubenko, I., Quetz, A., Oswald, I. W., McCandless, G. T., Chan, J. Y., Adams, P. W., Young, D. P., Ali, N., & Stadler, S. (2015). Hydrostatic pressure-induced modifications of structural transitions lead to large enhancements of magnetocaloric effects in mnnisi-based systems. *Physical Review B*, *91*(2), 020401. https://doi.org/10.1103/physrevb.91.020401

Seh, A. Q., & Gupta, D. C. (2020). Comprehensive DFT investigation of transition-metal-based new Quaternary Heusler alloys CoNbMnZ (Z = GE, Sn): Compatible for spin-dependent and thermoelectric applications. *RSC Advances*, *10*(71), 43870-43881. https://doi.org/10.1039/d0ra08007

Shao, Y., Lai, J., & Shek, C. (1996). Preparation of nanocomposite working substances for room-temperature magnetic refrigeration. *Journal of Magnetism and Magnetic Materials*, *163*(1-2), 103-108. https://doi.org/10.1016/s0304-8853(96)00337-x

Silva, J. H. (2017). *Nanostructuring Gd5 (Si, Ge) 4 Multifunctional Materials* (Doctoral dissertation, Universidade do Porto (Portugal)).

Smaïli, A., & Chahine, R. (1997). Composite materials for ericsson-like magnetic refrigeration cycle. *Journal of Applied Physics*, *81*(2), 824-829. https://doi.org/10.1063/1.364166

Sturm, S., Vogel, M., Köhler-Langes, F., Quint, W., Blaum, K., & Werth, G. (2017). High-precision measurements of the bound electron's magnetic moment. *Atoms*, *5*(4), 4. https://doi.org/10.3390/atoms5010004

Taskaev, S., Kuz'min, M., Skokov, K., Karpenkov, D., Pellenen, A., Buchelnikov, V., & Gutfleisch, O. (2013). Giant induced anisotropy ruins the magnetocaloric effect in gadolinium. *Journal of Magnetism and Magnetic Materials*, *331*, 33-36. https://doi.org/10.1016/j.jmmm.2012.11.016

Taskaev, S., Skokov, K., Karpenkov, D., Khovaylo, V. V., Ulyanov, M. N., Bataev, D., Pellenen, A., & Fazlitdinova, A. G. (2016). The effect of plastic deformation on magnetic and Magnetocaloric properties of Gd90Ga10 Alloy. *Materials Science Forum*, *845*, 56-60. https://doi.org/10.4028/www.scientific.net/msf.845.56

Terakura, K., Oguchi, T., Williams, A. R., & Kübler, J. (1984). Band theory of insulating transition-metal monoxides: Band-structure calculations. *Physical Review B*, *30*(8), 4734-4747. https://doi.org/10.1103/physrevb.30.4734

Tishin, A. M., Gschneidner, K. A., & Pecharsky, V. K. (1999). Magnetocaloric effect and heat capacity in the phase-transition region. *Physical Review B*, *59*(1), 503-511. https://doi.org/10.1103/physrevb.59.503

Toliński, T., Falkowski, M., Synoradzki, K., Hoser, A., & Stüßer, N. (2012). Magnetocaloric effect in the ferromagnetic GdNi4M (M=Al, SI) and antiferromagnetic NdNiAl4 compounds. *Journal of Alloys and Compounds*, *523*, 43-48. https://doi.org/10.1016/j.jallcom.2012.01.156

Tripathy, D., Adeyeye, A. O., & Singh, N. (2006). Magnetization reversal in half metallic Fe3O4 based pseudo spin valve nanomagnet arrays. *INTERMAG 2006 - IEEE International Magnetics Conference*. https://doi.org/10.1109/intmag.2006.376099

Tura, A., & Rowe, A. (2011). Permanent magnet magnetic refrigerator design and experimental characterization. *International Journal of Refrigeration*, *34*(3), 628-639. https://doi.org/10.1016/j.ijrefrig.2010.12.009

Vanderbilt, D. (1990). Soft self-consistent pseudopotentials in a generalized eigenvalue formalism. *Physical Review B*, *41*(11), 7892-7895. https://doi.org/10.1103/physrevb.41.7892

Vázquez, M., Jiménez, A., & Del Real, R. P. (2015). Controlled single-domain wall motion in cylindrical magnetic microwires with axial anisotropy. *Magnetic Nano- and Microwires*, (pp. 379-401). https://doi.org/10.1016/b978-0-08-100164-6.00012-6

Viglione, G. (2020). Ozone-depleting gases might have driven extreme Arctic warming. *Nature Climate Change*. *6*(3), 198-201. https://doi.org/10.1038/d41586-020-00108-2

Villarreal, O. D. (2016). *Theoretical and computational studies of the interactions between small nanoparticles and with aqueous environments*. The University of Texas at San Antonio.

Vollmer, M., & Möllmann, K. P. (2017). *Infrared thermal imaging: fundamentals, research and applications*. John Wiley & Sons.

Vosko, S. H., Wilk, L., & Nusair, M. (1980). Accurate spin-dependent electron liquid correlation energies for local spin density calculations: A critical analysis. *Canadian Journal of Physics*, *58*(8), 1200-1211. https://doi.org/10.1139/p80-159

Wada, H., & Tanabe, Y. (2001). Giant magnetocaloric effect of MnAs1−xSbx. *Applied Physics Letters*, *79*(20), 3302-3304. https://doi.org/10.1063/1.1419048

Wang, S. Q., & Ye, H. Q. (2003). *Ab initio* elastic constants for the lonsdaleite phases of C, SI and GE. *Journal of Physics: Condensed Matter*, *15*(30), 5307-5314. https://doi.org/10.1088/0953-8984/15/30/312

Warburg, E. (1881). Magnetische Untersuchungen. *Annalen der Physik*, *249*(5), 141-164. https://doi.org/10.1002/andp.18812490510

Wiendlocha, B., Tobola, J., Kaprzyk, S., Zach, R., Hlil, E. K., & Fruchart, D. (2008). Magnetocaloric properties of Fe2− xTxP (T= Ru and Rh) from electronic structure calculations and magnetization measurements. *Journal of Physics D: Applied Physics*, *41*(20), 205007. https://doi.org/10.1088/0022-3727/41/20/205007

Wilson, S. (1997). Practical AB initio methods for molecular electronic structure studies. IV. Relativistic many-body perturbation theory. *Problem Solving in Computational Molecular Science*, 185-213. https://doi.org/10.1007/978-94-009-0039-4_6

Womes, M., Karnatak, R., Esteva, J., Lefebvre, I., Allan, G., Olivier-Fourcades, J., & Jumas, J. (1997). Electronic structures of FeS and FeS 2 : X-ray absorption spectroscopy and band structure calculations. *Journal of Physics and Chemistry of Solids*, *58*(2), 345-352. https://doi.org/10.1016/s0022-3697(96)00068-6

Xu, K., Li, Z., Liu, E., Zhou, H., Zhang, Y., & Jing, C. (2017). Magnetocaloric effect and negative thermal expansion in hexagonal FE doped MnNiGe compounds with a magnetoelastic AFM-FM-like transition. *Scientific Reports*, *7*(1). https://doi.org/10.1038/srep41675

Yablonovitch, E., Gmitter, T., & Leung, K. (1991). Photonic band structure: The face-centered-cubic case employing nonspherical atoms. *Physical Review Letters*, *67*(17), 2295-2298. https://doi.org/10.1103/physrevlett.67.2295

Zhang, Y. J., Liu, Z. H., Wu, Z. G., & Ma, X. Q. (2019). Prediction of fully compensated ferrimagnetic spin-gapless semiconducting FeMnGa/Al/In half Heusler alloys. *IUCrJ*, *6*(4), 610-618. https://doi.org/10.1107/s2052252519005062

Zhao, N., Zhao, D., & Ma, H. (2012). Experimental investigation of magnetic Field effect on the magnetic Nanofluid oscillating heat pipe. *Volume 2: Heat Transfer Enhancement for Practical Applications; Fire and Combustion; Multi-Phase Systems; Heat Transfer in Electronic Equipment; Low Temperature Heat Transfer; Computational Heat Transfer*. https://doi.org/10.1115/ht2012-58170

Zimm, C., Boeder, A., Chell, J., Sternberg, A., Fujita, A., Fujieda, S., & Fukamichi, K. (2006). Design and performance of a permanent-magnet rotary refrigerator. *International Journal of Refrigeration*, *29*(8), 1302-1306. https://doi.org/10.1016/j.ijrefrig.2006.07.014

Zvyagin, A. A. (2017). Magnetic ordering of anisotropic magnets due to the rotation of a magnetic field. *Low Temperature Physics*, *43*(8), 960-964. https://doi.org/10.1063/1.5001296

APPENDICES

Appendix I: Publication

Investigation of magnetic properties of FeMnP1-xAx (A = In, Se and Sn, where x = 0.33) by use of GGA functionals

ELSEVIER

Investigation of magnetic properties of $FeMnP_{1-x}A_x$ (A = In, Se and Sn, where x = 0.33) by use of GGA functionals

Check for updates

Otieno Vincent, Winfred Mueni Mulwa [*], M.S.K. Kirui

Department of Physics, Egerton University, 536-20115, Egerton, Kenya

ARTICLE INFO

ABSTRACT

Magnetic properties of stable iron-based compounds ($FeMnP_{1-x}A_x$ (A = Si, In, Se and Sn) were investigated by use of Quantum Espresso (QE) within the Density Functional Theory (DFT) formalism as a viable magnetic refrigerant. In this research work, DFT technique was the first principle theoretical approach that was employed along with the planewave pseudopotentials (ultrasoft), and the projected augmented wave (PAW) within the generalized gradient approximation (GGA) to describe the electronic structure and investigation of magnetic properties. Magnetic stability is described as the repeated magnetic performance of a material under specific conditions over the life of a magnet. In this case our reference compound, $FeMnP_{0.67}Si_{0.33}$ was optimized and its properties were examined in both ferromagnetic (FM) and antiferromagnetic (AFM) states. Two Si atoms were later substituted with atoms of post-transitional metals in period four and five which has shown first-order magnetic transition at near room temperatures. In, Se and Sn were chosen to replace silicon since they would easily mimic the bond, their availability and nontoxic nature. The results showed that only ferromagnetic states of both host and doped compounds gave promising magnetic properties that can be applied in magnetocaloric effect phenomenon. Their band structure results indicated that they were all metals. Antiferromagnetic states showed no magnetic properties as the spin-polarized graph resulted in perfect symmetry of spin up projected density of states (PDOS) and spin down PDOS. From the thermo_pw calculations, it was realized that $FeMnP_{0.67}In_{0.33}$ is the best candidate for near room temperature magnetic refrigeration among the studied compounds.

Appendix II: Research Permit

REPUBLIC OF KENYA

NATIONAL COMMISSION FOR SCIENCE,TECHNOLOGY & INNOVATION

Ref No: **844189**

Date of Issue: **14/July/2021**

RESEARCH LICENSE

This is to Certify that Mr.. Vincent Otieno Odhiambo of Egerton University, has been licensed to conduct research in Nakuru on the topic: **Investigation of magnetic properties of Fe2MnP-based materials for near room temperature using Density Function Theory** for the period ending : 14/July/2022.

License No: **NACOSTI/P/21/11588**

844189

Applicant Identification Number

Director General
NATIONAL COMMISSION FOR
SCIENCE,TECHNOLOGY &
INNOVATION

Verification QR Code

NOTE: This is a computer generated License. To verify the authenticity of this document,
Scan the QR Code using QR scanner application.

66

Appendix III: Sample input file

```
&control
   calculation='scf'
   pseudo_dir = './'
   outdir='./'
   prefix='Fe2P'
 /
 &system
   ibrav = 4,
   celldm(1) = 10.981569882
   celldm(3) = 0.59
   nat= 9, ntyp= 4,
   ecutwfc = 90, ecutrho = 720
   occupations='smearing', smearing='mv', degauss=0.05


 /
 &electrons
   mixing_beta = 0.7
/
&IONS
trust_radius_max=0.2
/
&CELL
cell_dynamics='bfgs'
/
ATOMIC_SPECIES
Fe 55.85  fe_pbe_v1.5.uspp.F.UPF
Mn 54.94  mn_pbe_v1.5.uspp.F.UPF
P  30.97  p_pbe_v1.5.uspp.F.UPF
Si 28.09  si_pbe_v1.uspp.F.UPF
ATOMIC_POSITIONS {crystal}
Mn   0.000000 0.408468 0.500000
Mn   0.591532 0.591532 0.500000
Mn   0.408468 0.000000 0.500000
Fe   0.743444 0.000000 0.000000
Fe   0.256556 0.256556 0.000000
Fe   0.000000 0.743444 0.000000
P    0.666667 0.333333 0.000000
P    0.333333 0.666667 0.000000
Si   0.000000 0.000000 0.500000
K_POINTS (automatic)
3 3 5 0 0 0
```

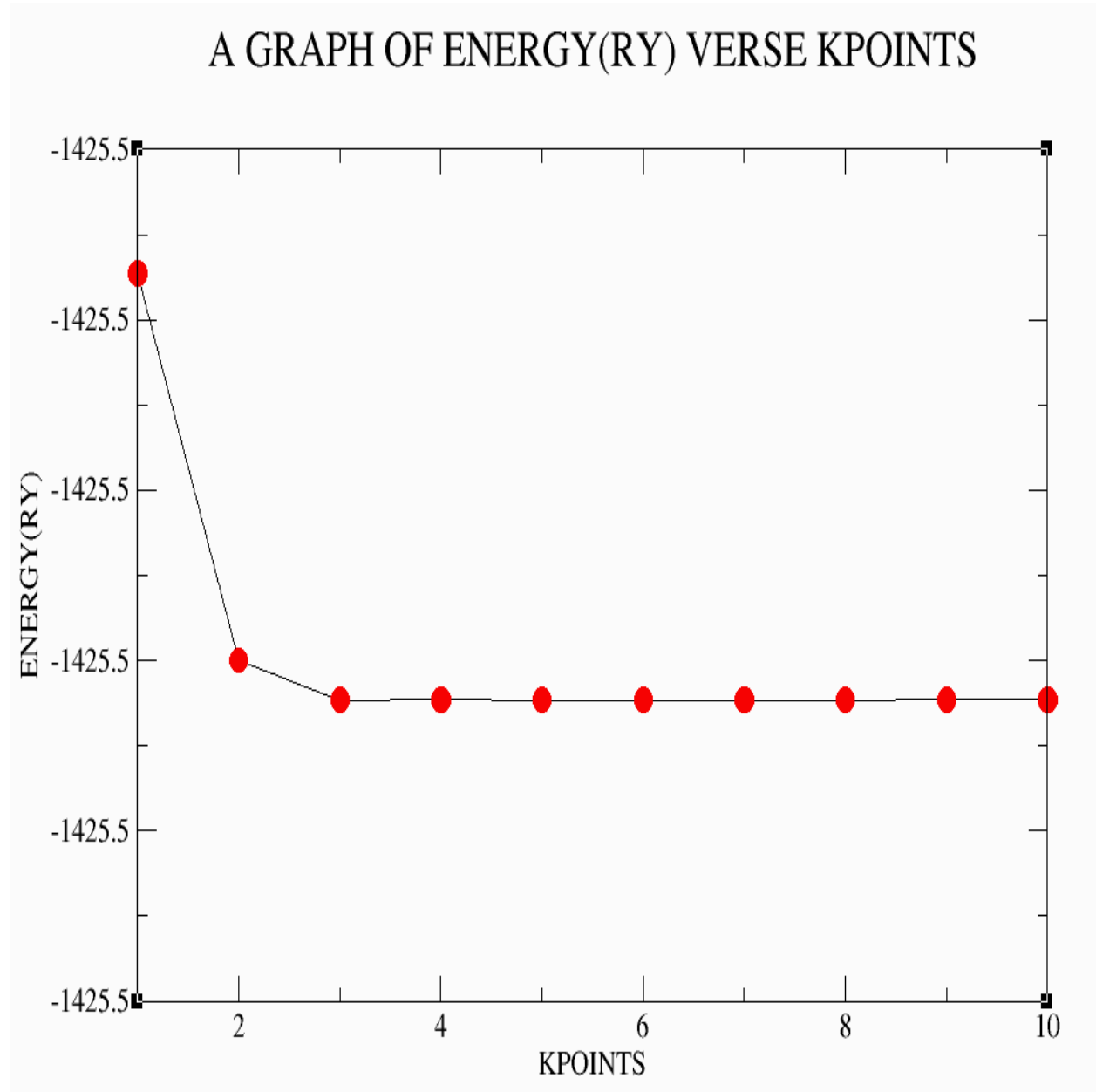**Crystal parameters**

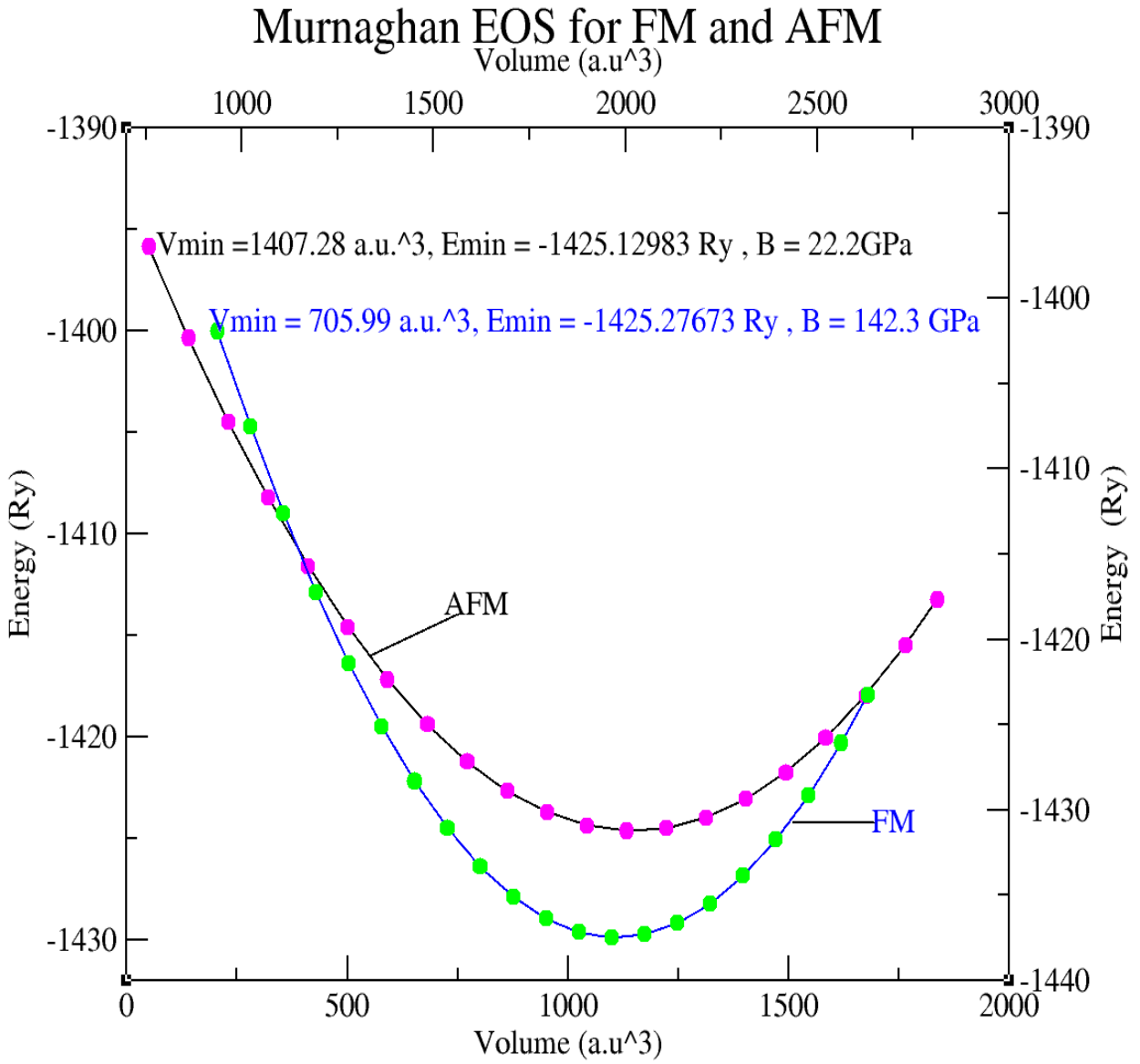For a hexagonal structure, a = b ≠ c
ak = 5.8111
ck = 3.4286
a = b = alat/ak
c = alat/ck

K-points optimization graph

A GRAPH OF ENERGY(RY) VERSE KPOINTS

Equation of state graph

Murnaghan EOS for FM and AFM

Relaxed AFM FeMnPIn Unit cell